Design of SiGe/Si Quantum-Well Optical Modulators

by

Tania Tasmin

B.Sc., Bangladesh University of Engineering and Technology, 2004

A THESIS SUBMITTED IN PARTIAL FULFILLMENT OF
THE REQUIREMENTS FOR THE DEGREE OF

MASTER OF APPLIED SCIENCE

in

The Faculty of Graduate Studies

(Electrical and Computer Engineering)

THE UNIVERSITY OF BRITISH COLUMBIA

(Vancouver)

August 2010

Abstract

An electro-optic modulator containing a single SiGe/Si quantum-well has been designed for operation at $\lambda_0 = 1.55$ μm. This single quantum-well modulator has a lower $V_\pi L_\pi$ than the 3 quantum-well modulator recently designed and optimized by Maine *et al.* for operation at $\lambda_0 = 1.31$ μm, for which the $V_\pi L_\pi$ product was 1.8 V·cm [25]. Both modulators are derived from the detailed design given for their modulator in [40]. This single quantum-well modulator contains a $Si_{0.8}Ge_{0.2}$ quantum-well with Non-Intentionally Doped (NID) and P^+ highly doped layers on either side. With no field applied, holes from the P^+ layers are captured by and confined in the quantum-well and when a reverse bias is applied holes are released from the quantum well and drift to the P^+ contact layer. Variations of the hole distribution lead to changes in the free-carrier absorption and the refractive index of each layer and subsequently to phase modulation of guided TE modes. The $V_\pi L_\pi$ product of the single quantum-well modulator is estimated 1.09 V·cm for low voltage linear modulation and 1.208 V·cm for 0 to 1.6 V digital modulation, whereas the 3 quantum-well modulator gives a $V_\pi L_\pi$ of 2.039 V·cm for 0 to 6 V digital modulation for operation at $\lambda_0 = 1.55$ μm. Also, the optical loss in the single quantum-well (5.36 dB/cm at $V = 0$ V) is lower than that of the 3 quantum-well structure (5.75 dB/cm at $V = 0$ V). This

single quantum-well modulator should also offer higher frequency operation than the 3 quantum-well modulator.

Table of Contents

List of Tables

List of Figures

Acknowledgements

I would like to express my profound gratitude to my thesis supervisor: Dr. Nicolas A. F. Jaeger for his friendly supervision and guidance throughout the course of this research work. He was always ready to offer timely suggestions and I have learned a lot from him.

Sincere and special thanks go to Dr. Lukas Chrostowski (my co-supervisor) and Dr. Nicolas Rouger for the endless discussions on problems I encountered during the course of this work. Without their support and kind guidance, I would not have made it as far as I did.

I am also grateful to Dr. Guangrui Xia for her valuable discussions and assistance.

I would also like to thank everybody who has contributed in one way or another to my experience at UBC: Dr. Jaeger's graduate students, Dr. Chrostowski's graduate students, Dr. Alina Kulpa.

I would like to thank my parents Md. Shafiqul Islam and Shahjat Merina for their prayers and encouragement and also my husband Sharif Fakhruz Zaman and my sweet daughter Sharif Maymunah Zaman for their support, love, and patience. I would also like to thank my grandmother Begum Fazilatunnesa for her love and prayers at every stage my life.

Above all, I give thanks to Allah, for the gift of life, with a bit of knowl-

edge and understanding and mercy.

Dedication

To my loving parents.

Statement of Co-Authorship

Chapter two and chapter three of this thesis will be published in SPIE Photonics North Proceedings, 2010. The authors are Tania Tasmin, Nicolas Rouger, Guangrui Xia, Lukas Chrostowski, and Nicolas A. F. Jaeger.

The literature review and the modeling for this research work were done by Tania Tasmin under the supervision of Dr. Nicolas Jaeger, Dr. Lukas Chrostowski, and Dr. Guangrui Xia. Tania Tasmin did the final preparation for the manuscript of the paper after careful revision and approval by Nicolas Rouger, Guangrui Xia, Lukas Chrostowski, and Nicolas A. F. Jaeger.

Chapter 1

Introduction

Today optical interconnects dominate long-distance communications due to their low transmission loss, high bandwidth, and immunity to interference. But, in the case of short distance communications, such as chip-to-chip and on-chip interconnects, the electrical interconnects (metal wires) still dominate. However, due to the dramatic increase in the number of transistors per chip and the shrinkage of the transistors, electrical interconnects encounter many problems such as RC propagation delays, signal distortion, and high power consumption. Thus with the transistors getting smaller, electrical interconnects have become the primary bottleneck for the improvement of the chip performance [1]. Optical interconnects offer a promising way to alleviate this bottleneck. The basic advantages of the optical interconnects over the electrical interconnects are reduced delay, lower power consumption, and higher bandwidth.

1.1 Motivation

The improvement of the modern technology leads a dramatic increase in the number of transistors per chip as well as the shrinkage of transistors on a microprocessor [2]. This shrinking process results in a spectacular im-

provement of the device speed. On the microprocessor, metallic (electrical) interconnects are used for signalling and clocking. Local interconnects, consisting of very thin conductors, are used to connect various parts of multiple transistors within a functional block on the chip. Global interconnects provide clock and signal distribution between different functional blocks on the chip and deliver power/ground to all of the functional blocks [3]. With the miniaturization of transistors on the chip, the length of the local interconnects scale down and propagation delay for the local interconnects is not an issue. But the cross-sectional area of the global interconnects reduce without changing the length which leads to the increase of the resistance of the global interconnect and hence the increase of RC propagation delays [4]. Other problems with electrical interconnects are the power consumption and the signal distortion. Thus with the transistor shrinking, electrical interconnects have become the primary bottleneck for improvement of the device performance [1]. Optical interconnects offer a promising way to alleviate this bottleneck. The basic advantages of the optical interconnects over the electrical interconnects are reduced RC delay, lower power consumption, and higher bandwidth, particularly for the longer distance interconnects (e.g. across the chip, between processor cores).

The basic building blocks of an optical interconnect system are light sources, modulators, waveguides, and detectors. Light sources can be either directly modulated (light source is turned on/off according to an electrical signal) or it can be used with an external modulator (light coming from the light source will be coupled with an external modulator and the light intensity at the modulator output is controlled by an applied electrical signal

to the modulator). Waveguides provide a means of carrying light from the light sources to the modulators and from the modulator to the detector or other parts of the chip. Detectors are used to convert the modulated light back into electrical signal.

Silicon-based materials are the best platform for the various components of on-chip optical interconnects. Due to their CMOS (Complementary Metal-Oxide-Semiconductor) compatibility, both the electronic circuit and photonic circuit can be grown monolithically on the same substrate, reducing the cost [5]. Moreover, stronger optical confinement can be obtained with SOI (Silicon-On-Insulator) waveguides due to the higher refractive index contrast between Si and SiO_2 as compared to those obtained with III-V based optical interconnects grown on Si substrates [6]. Significant progress has been made to develop Si-based, on-chip, optical components and, in particular, the light sources, the waveguides, and the photodetectors [2]. The main obstacle for implementing the optical interconnect system is developing a Si-based optical modulator with low drive voltage, small size, low optical loss, and high speed. In this thesis we have designed SiGe/Si quantum-well modulators having all these properties.

1.2 Optical Modulation in Si and Si-based Materials

Optical modulation is defined as the process of varying a property of light *e.g.*, phase, frequency, polarization, or intensity according to an applied electrical signal (*i.e.*, the process of impressing information on a light car-

rier). The optical modulators can be grouped into two major types: electro-absorption modulators and electro-optic modulators.

In an electro-absorption modulator, a variation of the light intensity at the modulator output, according to the applied electric field, is obtained through the variation of the optical absorption coefficient of the waveguide material. ON/OFF states correspond to the situation of low absorption coefficient and high absorption coefficient, respectively. In an electro-optic modulator, the phase of the carrier light is varied according to the applied electric field through the variation of the refractive index of the waveguide material. An integrated interferometer is typically used to convert the refractive index induced phase modulation into the intensity modulation.

The electro-absorption effect include the Franz-Keldysh effect and the quantum-confined Stark effect. The electro-optic effect include Pockels effect, Kerr effect, and free carrier absorption effect. The Pockels effect, in which the refractive index change of a material is linearly proportional to the applied electric field, is absent in Si. The Kerr effect, in which the refractive index change is proportional to the square of the applied electric field, is very small in Si as shown in Fig. 1.1 [7] . Hence, the Franz-Keldysh effect, the quantum-confined stark effect, and the free carrier absorption effect, which are the relevant optical modulation mechanisms in Si and Si-based materials, are described in section 1.2.1, 1.2.2, and 1.2.3, respectively.

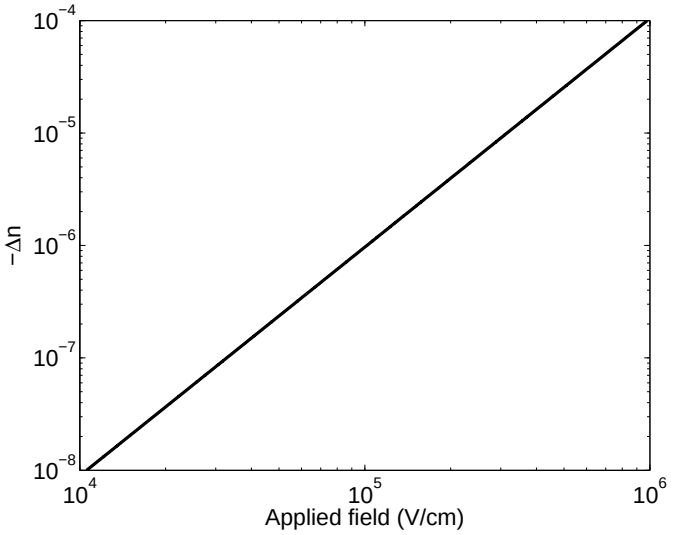

Figure 1.1: Kerr effect in c-Si, re-digitized from [7].

1.2.1 Franz-Keldysh Effect (FKE)

When a strong electric field is applied to a bulk semiconductor, the absorption coefficient of the semiconductor changes according to the applied electric field. Also, with the application of the electric field, there is a tilt in the valence band and in the conduction band. At some locations, the energy difference between the conduction band and the valence band is reduced (by dE) below the bandgap energy E_g. Photons with energy higher than $E_g - dE$ are absorbed at these locations by exciting the electrons from the valance band to the conduction band as shown in Fig. 1.2(a). So there is an absorption tail below the bandgap energy as shown in Fig. 1.2(b). This effect is known as Franz-Keldysh effect [4].

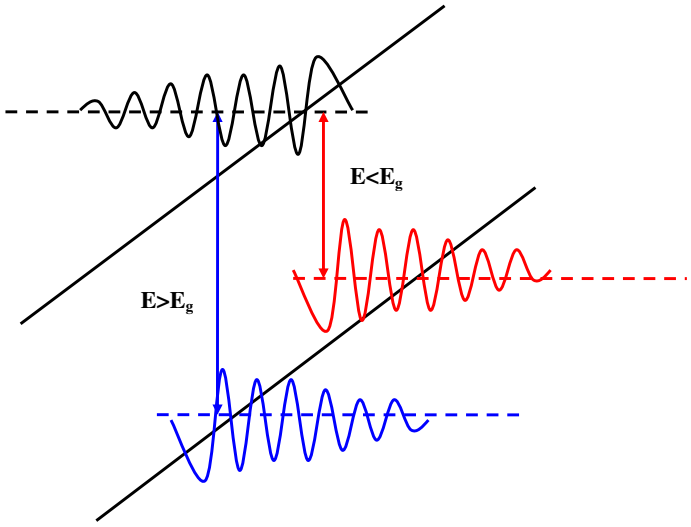

(a)

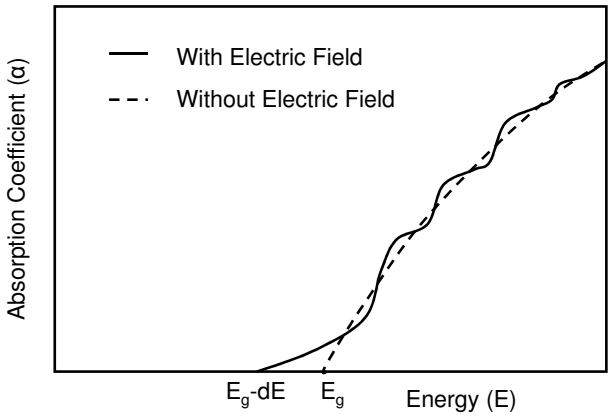

(b)

Figure 1.2: (a) Energy band diagram, (b) absorption spectrum in bulk semiconductor with and without the electric field.

The complex refractive index of a material can be written as $n + ik$, where n is the refractive index and k is the optical extinction coefficient. The absorption coefficient, α is related to k by $k = \alpha\lambda/4\pi$. The change in the real part of the refractive index (Δn) and in the imaginary part of the refractive index ($\Delta\alpha$) are related by the following Kramers-Kronig relations [7]

$$\Delta n(E) = \frac{c}{\pi} P \int_0^\infty \frac{\Delta\alpha(\bar{E})}{\bar{E}^2 - E^2}\, d\bar{E} \tag{1.1}$$

$$\Delta\alpha(E) = -\frac{c}{\pi} P \int_0^\infty \frac{\Delta n(\bar{E})}{\bar{E}^2 - E^2}\, d\bar{E} \tag{1.2}$$

The absorption change with the applied electric field is obtained by

$$\Delta\alpha(E, \xi) = \alpha(E, \xi) - \alpha(E, 0) \tag{1.3}$$

where E is the energy of the light and ξ is the applied electric field. Hence, in the Franz-Keldysh effect, the electric field involves a change in both the absorption coefficient and in the refractive index. Soref and Benett [7] quantified the change in the refractive index in silicon using the electro-absorption spectrum measured by Wendland and Chester [8]. They plotted the change in refractive index as a function of the applied electric field (Franz-Keldysh effect) at $\lambda_0 = 1.07$ μm and at $\lambda_0 = 1.09$ μm which are shown in Fig. 1.3. The Franz-Keldysh effect falls very significantly at the telecommunication wavelength, so this effect is not a favourable choice for the silicon electro-optic modulators.

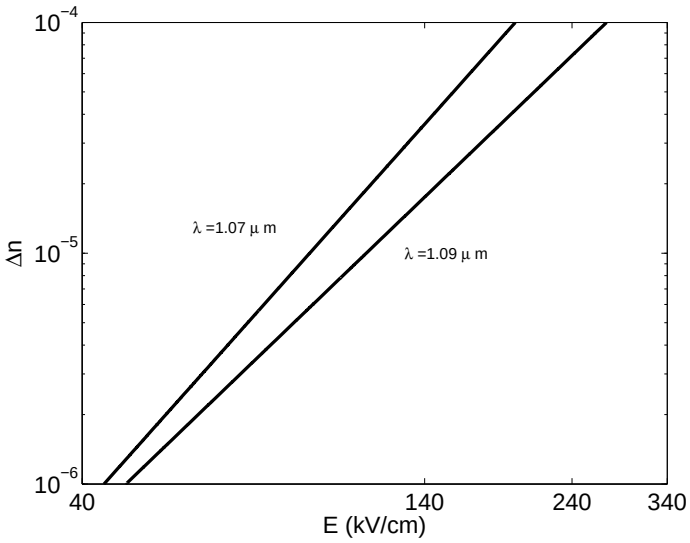

Figure 1.3: Field dependence of refractive index change at two wavelengths, re-digitized from [7].

1.2.2 Quantum-Confined Stark Effect (QCSE)

In a quantum-well, when no electric field is applied, the electron and the hole wavefunctions are symmetrical inside the well and electron-hole are coupled together by coulombic forces to form excitons. These excitons give sharp resonance peaks at the band-edge of the absorption spectrum in absence of an electric field. With the application of the electric field, the quantum-well energy decreases with respect to the center of the well and electron and hole wavefunctions shift towards the opposite sides of the quantum-well. Due to the electron and hole separation in the quantum-well, the exciton peak is lowered at the band-edge and the band-edge is shifted towards the long wavelength (red shifting) [4].

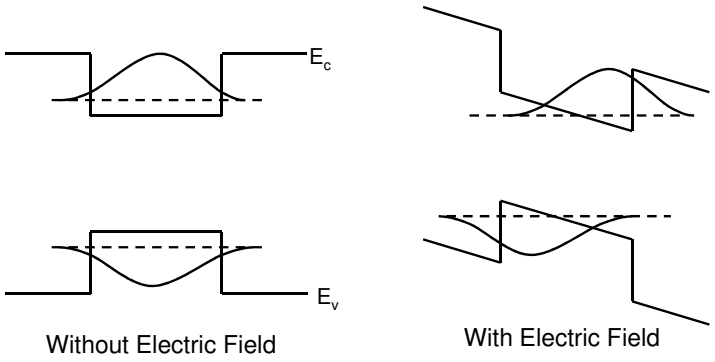

Figure 1.4: Quantum-well wavefunctions with and without electric field.

Recently the discovery of strong QCSE is reported in compressively strained Ge quantum-wells with SiGe barriers [9]. We will discuss about

this electro-absorption modulator in section 1.3.

1.2.3 Free Carrier Absorption Effect

If the energy of the incident light is so small that the photons cannot transfer electrons from the valence band to the conduction band, electrons (or holes) undergo transitions within different states in the same band by absorbing the incoming light. This is known as the free carrier absorption [10]. The free carrier absorption depends on the free carrier concentration of the material. If carriers are injected to an undoped sample, the absorption coefficient of that material increases and the refractive index decreases [11]. If the carriers are removed from a doped sample, the opposite effect takes place. As the refractive index change depends on both the frequency of light and the plasma of free carriers, this absorption is also called as plasma dispersion effect.

In classical physics, free carriers (electrons and holes) are treated as particles, and they are forced into motion by the incoming light. The displacement vector of the carriers, which is related to the electric field of the light, can be found by solving the equation of motion of the carriers. By putting this value of the displacement vector into the equation for dielectric permittivity, the formula for free-carrier-induced absorption change and the refractive index change are found as [12, 13]

$$\Delta\alpha = \frac{\lambda^2 e^3}{4\pi^2 c^3 n \epsilon_0} \left(\frac{\Delta N_e}{\mu_e m_e^{*2}} + \frac{\Delta N_h}{\mu_h m_h^{*2}} \right) \tag{1.4}$$

$$\Delta n = \frac{\lambda^2 e^2}{8\pi^2 c^2 n \epsilon_0} \left(\frac{\Delta N_e}{m_e^*} + \frac{\Delta N_h}{m_h^*} \right) \tag{1.5}$$

here e is the charge of an electron, ϵ_0 is the free space permittivity, n is the unperturbed refractive index, ΔN_e and ΔN_h are the change of concentration of free electrons and holes, respectively; m_e^* and m_e^* are the effective masses of electron and hole respectively and μ_e and μ_h are the mobilities of electrons and holes, respectively. However, these equations (defined as the Drude model) for free carrier absorption ignore all of the scattering process involving phonons or other impurities for conservation of momentum. Later Soref and Benett collected some experimental results [14–16] on the absorption spectrum of doped silicon (which are shown in Fig. 1.5), which include all of the scattering effects on the change of free carrier absorption.

From these curves they calculated the change in free carrier absorption and from the change in absorption they calculated the change in refractive index using the Kramers-Kronig relations. Then they used these results to determine the carrier-concentration dependence of the refractive index change at two specific wavelengths: $\lambda = 1.3$ and 1.55 μm, which are shown in Fig. 1.6(a) and Fig. 1.6(b), respectively.

From these figures, they concluded that the free holes are more effective in perturbing the refractive index than the free electrons. They also produced the following expressions, which are now used almost universally to evaluate changes due to injection or depletion of free carriers in silicon:

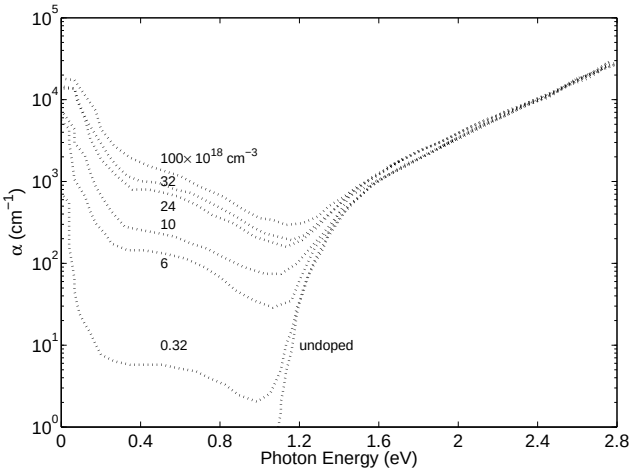

(a)

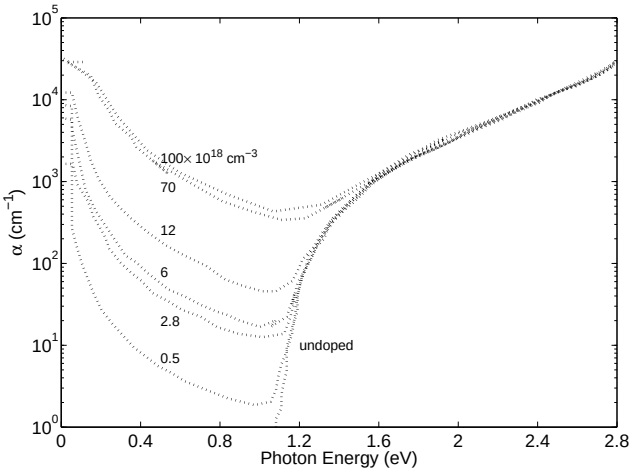

(b)

Figure 1.5: Optical absorption of c-Si showing the influence of various concentrations of (a) free electrons (b) free holes, re-digitized from [7].

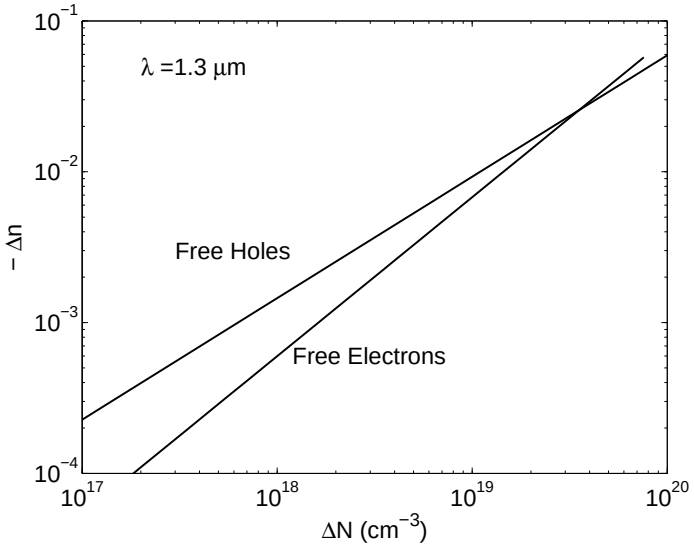

(a)

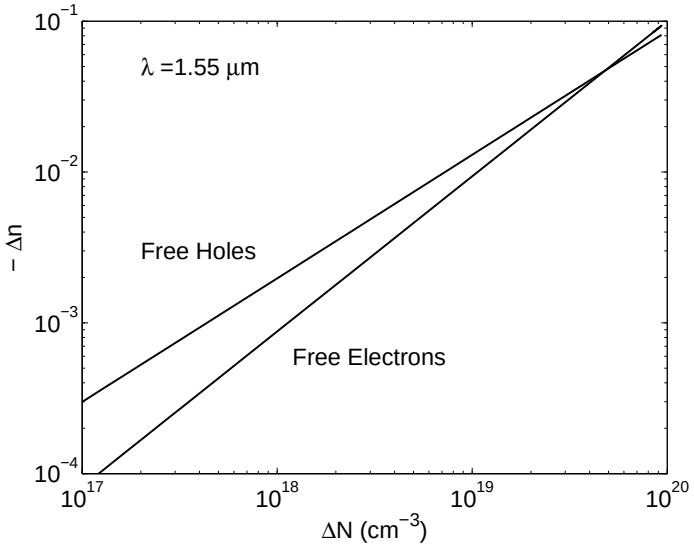

(b)

Figure 1.6: Refractive index perturbation in c-Si produced as a function of free carrier concentration at (a) $\lambda = 1.3$ μm, (b) $\lambda = 1.55$ μm, re-digitized from [7].

At $\lambda_0 = 1.3$ μm

$$\Delta\alpha = 5.9 \times 10^{-18}\Delta N + 4.0 \times 10^{-18}\Delta P \tag{1.6}$$

$$\Delta n = -6.2 \times 10^{-22}\Delta N - 6.0 \times 10^{-18}\Delta P^{0.8} \tag{1.7}$$

At $\lambda_0 = 1.55$ μm

$$\Delta\alpha = 8.5 \times 10^{-18}\Delta N + 6.0 \times 10^{-18}\Delta P \tag{1.8}$$

$$\Delta n = -8.8 \times 10^{-22}\Delta N - 8.5 \times 10^{-18}\Delta P^{0.8} \tag{1.9}$$

where ΔN and ΔP are, respectively, the electron and the hole concentration variations cm^{-3} with respect to the intrinsic carrier concentration.

1.3 Silicon Modulators Based on FKE, QCSE, and Free Carrier Absorption Effect

Table 1.1 summarized the recently reported SiGe electro-absorption modulators based on FKE and QCSE. Typically electro-absorption modulators suffer from chirp which can be reduced by using electro-optic modulators as these modulators can be implemented in a Mach-Zehnder push-pull configuration.

To date, the free carrier absorption effect has been the most effective

Group	Kimerling [17]	David Miller [9]
Publication Year	2008	2007
Modulation Mechanism	Franz-Keldysh effect	Quantum Confined Stark effect
Operating Wavelength	$1539 - 1553$ nm	$1441 - 1461$ nm
Structure	Reverse biased P-I-N diode grown on a SOI substrate. The intrinsic region contains a 50 μm long, 600 nm wide and 400 nm high $Si_{0.08}Ge_{0.92}$ epitaxial layer. This layer is coupled with Si waveguides at the input and output.	Reverse biased P-I-N diode grown on a $Si_{0.1}Ge_{0.9}$ buffer on a Si substrate. The intrinsic region contains 40 pairs of compressively strained Ge/SiGe quantum-wells (15.5 nm Ge well/33 nm $Si_{0.16}Ge_{0.84}$ barrier).
Interferometric Structure	-	Fabry-Perot cavity
Insertion Loss	3.7 dB at 1550 nm	-
Extinction Ratio	8 dB at 1550 nm with 7 V	Peak contrast ratio 7.3 dB at 1457 nm for 0 to 10 V swing
3 dB Bandwidth	1.2 GHz	-

Table 1.1: Si electro-absorption modulators

mechanism for varying the refractive index in silicon, which is polarization independent [18]. Carrier injection, carrier depletion, and carrier accumulation are the most commonly used mechanisms that modify the free carrier concentration in Si modulators based on free carrier absorption [19] . Three different device configurations, namely, P-Intrinsic-N (P-I-N) diodes, PN diodes or metal-oxide-semiconductors field-effect transistors (MOSFET) are used to exploit these mechanisms.

In carrier-injection based modulators, free carriers are injected into the intrinsic region of a P-I-N diode by forward biasing the diode. The change

in free carriers leads to an increase in the absorption coefficient as well as a decrease in the refractive index of the device. These devices require a large forward bias current density to ensure significant carrier concentration change. Moreover, these devices have moderate response time (>> 1 ns) due to the electron-hole recombination process. In carrier-depletion based modulators, carriers are stored in the active region of a PN/P-I-N diode without an applied field, carriers are swept out of the active region by reverse biasing the diode. The change in free carrier leads to a decrease in the absorption coefficient as well as an increase in the refractive index of the device. In these modulators, only one kind of carrier (either electron or hole) is involved. Hence, no recombination process takes place and a high frequency can be expected from these devices. Moreover, current density is reduced in these devices which leads to the reduced power consumption as compared to the carrier-injection based devices. In case of the carrier-accumulation based devices, charge carriers are accumulated near the gate dielectric in a MOS capacitor when a voltage is applied to the device.

Table 1.2 summarized the recently reported Si modulators based on the free carrier absorption effect.

Table 1.2: Free carrier absorption based silicon modulators

Group	**Manipatruni** [20]	**Liao [21]**	**Liao [22]**
Publication Year	2007	2005	2007
Result Type	Modeling	Experimental	Experimental
Operating Wavelength	-	-	1550 nm
Carrier Density Variation by-	Injection	Accumulation	Depletion
Modulator Structure	PIN diode integrated with Si rib waveguide	MOS capacitor integrated with Si rib waveguide	PN diode integrated with Si rib waveguide
Interferometer	Ring resonator	MZI with 13 mm phase shifter	MZI with 5 mm phase shifter
$V_\pi \cdot L_\pi$	-	3.3 V·cm	4.0 V·cm
Phase shifter loss	-	10 dB	7 dB
3 dB Bandwidth	40 Gbps	RC cut-off frequency 10.2 GHz	20 GHz
Table continued on next page			

Table continued from previous page			
Group	**Marris [23]**	**Marris[24]**	**Marris [25]**
Publication Year	2006	2008	2008
Result Type	Experimental	Experimental	Modeling
Operating Wavelength	1550 nm	1550 nm	1310 nm
Carrier Density Variation by-	Depletion	Depletion	Depletion
Modulator Structure	Vertical PIN diode grown on SOI substrate, a highly doped P^+ layer embedded in the intrinsic region	Lateral PIN diode grown on SOI substrate, a highly doped P^+ slit embedded in the intrinsic region	Vertical PIN diode grown on SOI substrate, The intrinsic region consists of three $Si_{0.8}Ge_{0.2}$/Si quantum-well surrounded by P^+ highly doped layers.
Interferometer	Fabry-Perot cavity	MZI with 4 mm phase shifter	phase shifter length 3 mm
$V_\pi \cdot L_\pi$	3.1 V·cm (1 V·cm by simulation)	5.0 V·cm (2 V·cm by simulation)	1.8 V·cm
Phase shifter loss	-	5 dB	9 dB
3 dB Bandwidth	90 GHz by simulation	10 GHz	RC cut-off frequency 16 GHz

The change in free carrier concentration in these devices leads to the change in free carrier absorption which, in turn, changes the refractive index of the device. The phase of the light passing through the device will be changed due to the change in refractive index. This phase modulator can be converted into intensity modulator using a Mach-Zehnder interferometer structure, Fabry-Perot cavity structure, or ring resonator structure. The operating principles of these intensity modulators are described in section 1.3.1, section 1.3.2, and section 1.3.3, respectively.

1.3.1 Mach-Zehnder Interferometer

An integrated Mach-Zehnder interferometer consists of an input waveguide, a splitter, two phase shifters, an output combiner, and an output waveguide, as illustrated in Fig. 1.7. The optical beam coming through the input waveguide is split into two optical beams by the splitter. The two optical beams travel through the two phase shifters inserted into the arms of the Mach-Zehnder interferometer, and then recombine at the output combiner. The ON state is achieved when the two optical beams arrive at the combiner in phase and interface constructively to produce a high intensity. When an electric field is applied to the phase shifters to create a relative path difference between the two optical beams, the intensity is reduced. The OFF state is achieved when there is a differential phase shift of π *radians* and a minimum intensity is produced at the output. The splitter (or the combiner) can be either an optical Y-branch or a 3-dB coupler.

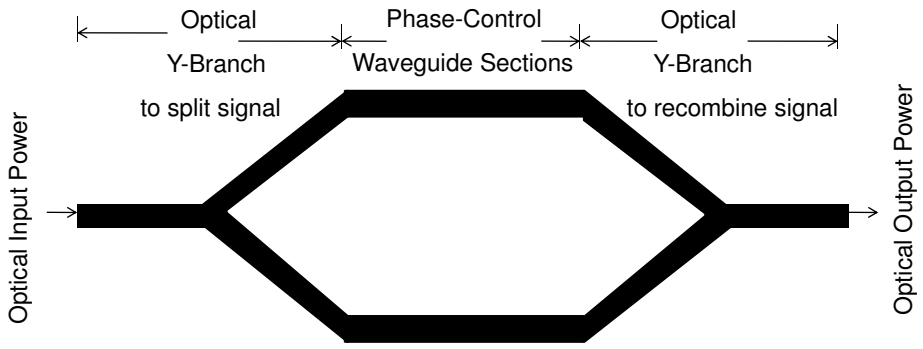

Figure 1.7: Schematic view of the Mach-Zehnder interferometer. Two optical Y-branch couplers are used to split and recombine the incoming light.

1.3.2 Fabry-Perot Interferometer

A Fabry-Perot cavity consists of two partially reflecting mirrors enclosing a resonator cavity as shown in Fig. 1.8. The transmission of the cavity will be maximum when the optical length of the cavity matches the resonance condition: $nL = p\lambda/2$, where n and L are, respectively, the refractive index and the length of the cavity, and p is an integer. The phase shifter is inserted into the cavity. When no bias is applied to the phase shifter, the transmission presents sharp maxima at some wavelengths. When a bias is applied to the phase shifter, the resonance condition modifies due to the change of the refractive index n, the resonance (resonant wavelengths are shifted) is shifted, and the cavity transmission at a given wavelength varies.

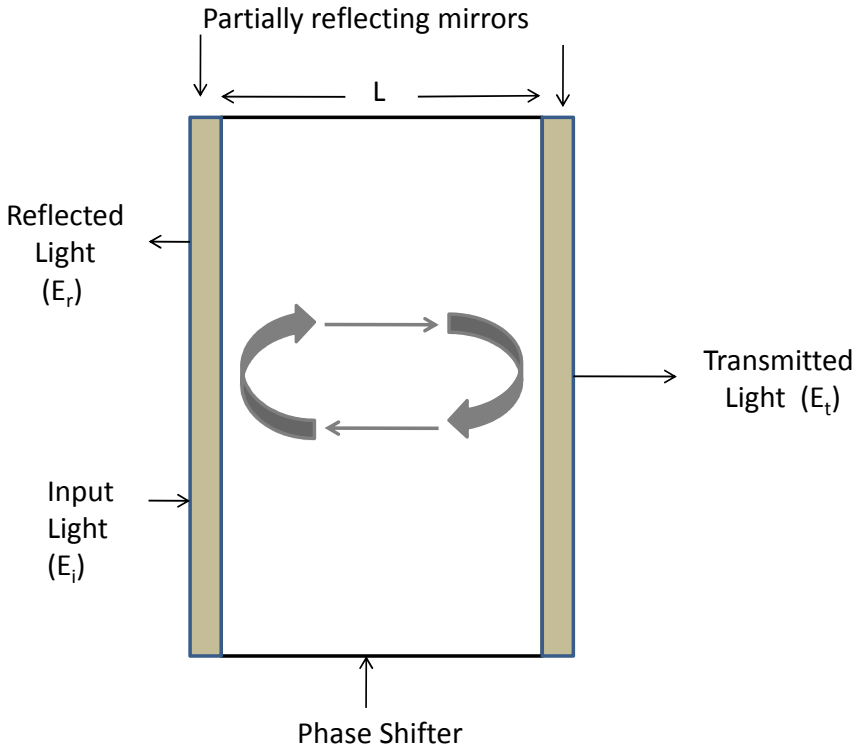

Figure 1.8: Schematic view of the Fabry-Perot cavity.

1.3.3 Ring Resonator

A ring resonator is based on a ring waveguide near a straight waveguide. To realize an optical modulator, the phase shifter is inserted in the ring. Light coming from the straight waveguide is coupled into the ring. The coupling of light from the straight waveguide to the ring depends on the gap between the waveguides. After propagating in the ring, light is coupled back to the straight waveguide. The transmission from the ring will be minimum

when the ring circumference matches the resonance condition: $nd = p\lambda/2$, where n and d are, respectively, the refractive index and the circumference of the ring, and p is an integer. When no bias is applied to the phase shifter integrated in the ring, the transmission presents sharp minima at some wavelengths. When a bias is applied to the phase shifter in the ring, the phase shift that is encountered by the optical mode propagating in the ring varies, and the resonance (resonant wavelengths are shifted) is shifted, and the transmission from the ring at a given wavelength varies.

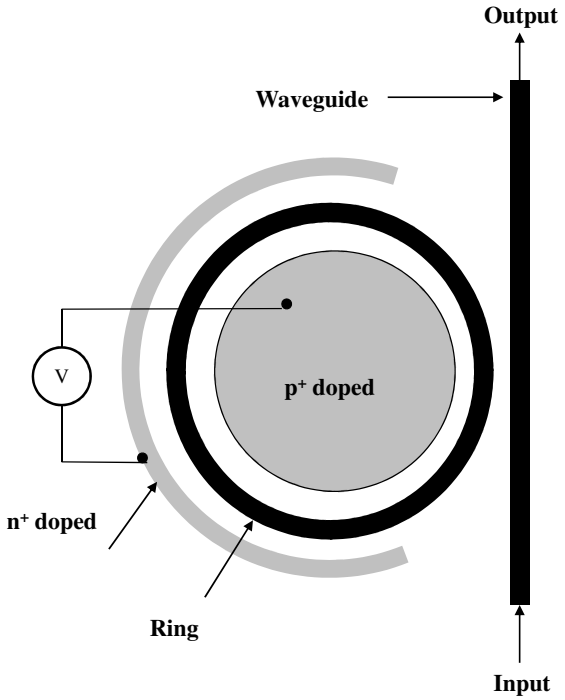

Figure 1.9: Schematic view of the ring resonator.

1.4 Organization of the Thesis

In this chapter, in order to provide some background, we have discussed various relevant optical modulation techniques in Si and the optical modulators based on them. At the beginning of this chapter, the Franz-Keldysh effect, the Quantum Confined Stark effect, and the free carrier absorption effect were discussed. Then, various techniques for obtaining optical modulation from Si and Si-based materials using free carrier absorption effect (*i.e.*, carrier injection, carrier depletion, and carrier accumulation) as well as a literature review of Si-based optical modulators using these techniques were presented. At the end of this chapter, the various interferometer structures used to obtain intensity modulation from Si-based phase modulators were briefly discussed.

In Chapter 2, **Material Choice, Device Structure, and Electrical and Optical Simulations**, we will describe the key components for designing SiGe/Si quantum-well modulators based on the free carrier depletion effect. The electrical and optical properties of Si and SiGe, which are important for designing these modulators, will be discussed at the beginning of Chapter 2. The software used for the electrical simulation of these modulators and the models used in this simulation will be described next. Then, we discussed the mode solver program used for the optical simulation of SiGe/Si waveguide modulators. The general structure of a $Si_{0.8}Ge_{0.2}$/Si quantum-well phase modulator followed by the coupled electrical-optical analysis used to design these modulators is presented next. Using this analysis, we simulated a 3 quantum-well $Si_{0.8}Ge_{0.2}$/Si modulator (designed by Marris *et al.*)

providing the most important results of the simulations. From the results of the DC analysis and the transient analysis performed on this 3 quantum-well modulator, we came to the conclusion that, a single quantum-well modulator may have a lower drive voltage, lower optical loss, and be capable of higher intrinsic speed than the 3 quantum-well modulator. Hence we removed 2 quantum-wells from the 3 quantum-well modulator and designed a single quantum-well modulator which will be described in Chapter 3.

In Chapter 3, **Single Quantum-Well SiGe/Si Optical Modulator**, the results of the simulation on a single quantum-well $Si_{0.8}Ge_{0.2}$/Si modulator, which is derived from the 3 quantum-well modulator described in Chapter 2, will be discussed. Then we will compare its performance with that of the 3 quantum-well modulator and we will find that, this single quantum-well modulator is better than the 3 quantum-well modulator in terms of the drive voltage, the optical loss, and the intrinsic speed. The performance of a Mach-Zehnder interferometer using single quantum-well phase modulators inserted into the two branches of the Mach-Zehnder interferometer will be described next. This chapter will conclude with the idea that, if we want to operate in a lower bias region, we can remove the quantum-wells and only the highly doped P^+ layers and the NID layers are sufficient to obtain an effective index variation close to that obtained with the 3 quantum-well or single quantum-well modulator in a lower bias region ($V < 2$ V). Removing the quantum-wells from the modulator may also increase the intrinsic speed.

Chapter 4, **Summary, Conclusion, and Suggestions for Future Work**, will summarize our present work and will give some suggestions

about the future work in this area.

Chapter 2

Material Choice, Device Structure, and Electrical and Optical Simulations

In this chapter, we describe the key components for designing a free carrier depletion based phase modulator. The material parameters choice which ensure various critical characteristics of a free carrier depletion based phase modulator are described in section 2.1. The software used for the electrical simulation for designing these modulators is described in section 2.2. A simple single mode SOI waveguide followed by the description of the mode solver used to solve for the eigen modes in these SOI waveguides are described in section 2.3. In section 2.4 the general structure of the free carrier depletion based phase modulators that we studied for operation at $\lambda_0 = 1.55$ μm is described. The coupled electrical-optical analysis used to design these modulators are also described in section 2.4. In the next section we describe a 3 quantum-well $Si_{0.8}Ge_{0.2}$/Si optical modulator. The results obtained using the DC analysis for the 3 quantum-well modulator is presented in section 2.5. This chapter concludes with section 2.6, which describes the transient

analysis performed on this 3 quantum-well $Si_{0.8}Ge_{0.2}$/Si electro-optic modulator.

To date, the free-carrier depletion effect has become the most commonly used approach to obtain the electro-optic effect in Si-based materials. The performance of different Si electro-optic modulators is compared in terms of the $V_\pi L_\pi$ product (V_π and L_π are, respectively, the applied voltage and the corresponding length required to obtain a change in the phase at the output of the modulator of π), the optical loss of the device, and the 3 dB bandwidth of the device. The $V_\pi L_\pi$ product is commonly used as the figure of merit for these devices [21–25]. An efficient modulator should possess a low $V_\pi L_\pi$ (for low drive voltage and/or small size) with low absorption losses and a high 3 dB bandwidth. L_π can be calculated from the formula $L_\pi = \lambda_0/2\Delta n_{\text{eff}}$ where, Δn_{eff} is the effective index variation at the applied bias of V_π. If these electro-optic modulators are inserted into two arms of a Mach-Zehnder interferometer as described in section 1.3.1, two additional performance parameters - insertion loss and extinction ratio, should be considered. The insertion loss and the extinction ratio are given by the following relations, I_{IN}, I_{ON}, $I_{Out-max}$ are defined as the the light input intensity, light output intensity and the maximum value of the light intensity that can be obtained at the output.

$$IL = 10 \times Log(\frac{I_{Out-max}}{I_{IN}}) \tag{2.1}$$

$$ER = 10 \times Log(\frac{I_{ON}}{I_{OFF}}) \tag{2.2}$$

In this chapter we describe the steps for designing a free carrier depletion based phase modulator and design an efficient 3 quantum-well $Si_{0.8}Ge_{0.2}$/Si electro-optic modulator which ensures low $V_\pi L_\pi$ product, low absorption losses, and high 3 dB bandwidth.

2.1 SiGe/Si Heterostructure Properties

In section 2.1.1 the reasons for choosing the Ge mole fraction, x, of 0.2 in a $Si_{1-x}Ge_x$ layer grown on a Si substrate are presented. To begin with, the bandgap requirements of the materials that will be used in a free carrier depletion based modulators are described. Then, why the thickness of the layers grown from these materials should be below a particular thickness, critical thickness, is discussed. How a Ge mole fraction of 0.2 meets both the bandgap and thickness requirements is presented next. This section concludes with the bandgap structure of a $Si_{0.8}Ge_{0.2}$/Si quantum-well. Section 2.1.2 describes two important properties (refractive index and absorption coefficient) of Si and SiGe.

2.1.1 Bandgaps and Band Alignments for SiGe/Si Heterostructure

Si and SiGe are both indirect bandgap materials. As absorption of photons by the free carriers within the same band is the desired mechanism to change the refractive index in silicon, band-to-band absorption of the light propagating through the device should be avoided. This is done by keeping the indirect bandgap of both Si and SiGe above the incident photon energy (0.95

eV at $\lambda_0 = 1.31$ μm and 0.801 eV at $\lambda_0 = 1.55$ μm) [26]. This condition is fulfilled by silicon (indirect bandgap of 1.12 eV). For a SiGe layer grown on a Si layer, the mole fraction of Ge in the SiGe layer should be chosen such that the bandgap of SiGe will be higher than the incident photon energy.

When a SiGe layer is grown on a Si layer, the thickness of the SiGe layer should be below a particular thickness to avoid misfit dislocations in SiGe layers. This thickness is known as critical thickness. If a SiGe layer with a thickness below the critical thickness [27] is grown on a Si layer to create a heterojunction device, due to the lattice mismatch between SiGe and pure Si, the SiGe films are biaxially strained [27]. This strain has two components; the hydrostatic component and the uniaxial component. The hydrostatic component lowers the conduction band minimum and lifts the valence band maximum, as a result band gap energy will be decreased in the strained SiGe layers [27]. The uniaxial component splits the valence band into a heavy hole band and a light hole band where light hole band becomes the topmost (lowest energy) valence band [4]. Once the critical thickness is exceeded, these films go back to their intrinsic cubic lattice constant and misfit dislocations appear in the films. These misfit dislocations degrade the optical and electrical quality of these films. In order to avoid these misfit dislocations occuring, the thickness of the SiGe layer should be below the critical thickness. This critical thickness depends on the Ge mole fraction as shown in Fig. 2.1 [28]. In a Si/SiGe/Si multilayer structure, in case of p periods of Si (thickness d_{Si}) and $Si_{1-x}Ge_x$ layer (thickness d_{SiGe}), the critical thickness can be evaluated by considering an equivalent structure of a single layer $Si_{1-x'}Ge_{x'}$, whose Ge content is given by $x' = x(d_{SiGe})/(d_{SiGe} + d_{Si})$

and thickness is given by $p(d_{SiGe} + d_{Si})$ [26]. For example, if a Si/SiGe/Si multilayer structure is grown with Si thickness of $d_{Si} = 25$ nm, SiGe thickness of $d_{SiGe} = 10$ nm, and the Ge mole fraction of 0.2, the equivalent layer has a Ge fraction $x^{'} = 0.06$. This leads to a critical thickness for such a Si/SiGe/Si multilayer structure about 125 nm as shown in Fig. 2.1. The total thickness of the Si/SiGe/Si multilayer structure ($p(d_{SiGe} + d_{Si})$) must be below 125 nm to avoid misfit dislocations in the SiGe layers.

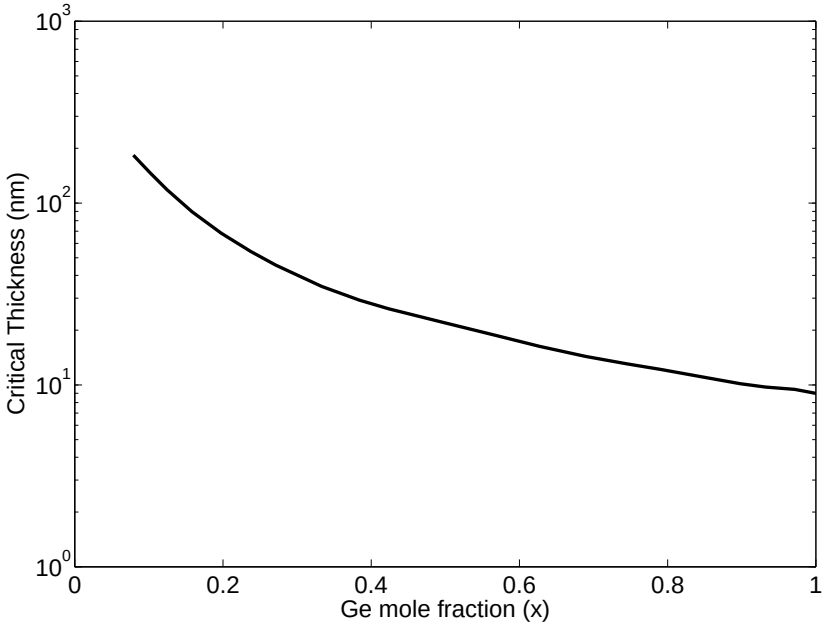

Figure 2.1: Critical layer thickness of SiGe layer grown on Si as a function of the Ge mole fraction, re-digitized from [28].

The bandgap relation of strained $Si_{1-x}Ge_x$ is given by [26] $E_g = 1.12 - 0.74x$. For the Ge mole fraction of 0.2 in $Si_{1-x}Ge_x$, the bandgap of SiGe will be 0.972 eV, which is above the incident light energy (0.95 eV at $\lambda_0 = 1.31$

μm and 0.801 eV at $\lambda_0 = 1.55$ μm). Thus the bandgap requirement is fulfilled. Now, for a multiple periods of SiGe/Si layers, the critical thickness depends on both the Ge mole fraction and the the thicknesses of Si and SiGe layers. We have seen that with $d_{Si} = 25$ nm and $d_{SiGe} = 10$ nm, if the Ge mole fraction of 0.2 is selected, the critical thickness is about 125 nm. In section 2.4, we will see that the thickness of the Si/SiGe/Si multilayer structure will be much lower than this thickness.

At the heterojunction, the conduction band discontinuity is given by $\Delta E_c < 20$ meV and the valence band discontinuity is given by $0.74x$ in [26]. The band alignment of a $Si_{0.8}Ge_{0.2}$/Si heterostructure grown on a Si substrate, that we used in our simulations, is shown in Fig. 2.2. The valence band and conduction band discontinuities that we used in our simulation are quite similar to those used in [26]. For the high valence band discontinuity, a $Si_{0.8}Ge_{0.2}$ layer sandwiched between Si layers acts as the well for holes. When no voltage is applied to this structure, holes will be confined inside the SiGe wells and, when a reverse bias voltage is applied, they will escape from the SiGe wells. Both the confinement of holes inside the quantum-wells at $V = 0$ V and the depletion of holes at a particular reverse voltage are important for getting larger changes of the refractive index in the SiGe layers, which will lead to higher effective index variations.

2.1.2 Refractive Index and Absorption Coefficient

The refractive index of strained $Si_{0.8}Ge_{0.2}$ is given in [29] by

$$n_{SiGe}(x, \lambda_0) = n_{Si}(\lambda_0) + (1.16 - 0.26 \cdot \lambda_0) \times x^2 \tag{2.3}$$

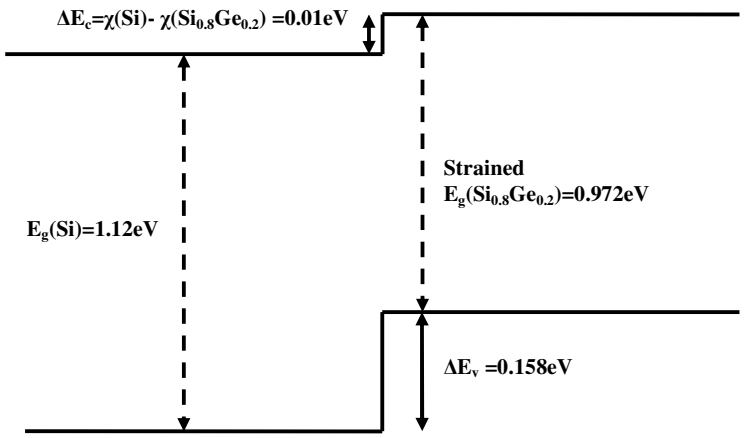

Figure 2.2: Band alignments for $Si_{1-x}Ge_x$/Si heterostructures on Si substrate, where χ is the electron affinity.

where x is the Ge mole fraction in $Si_{1-x}Ge_x$. This expression is applicable for wavelengths from 0.9 to 1.7 μm and for mole fractions less than 0.33. In our simulation, the refractive index of intrinsic Si is taken to be 3.503 and 3.475 at the wavelengths 1.31 and 1.55 μm, respectively. The absorption coefficient for the undoped Si and SiGe which can be extracted from Fig. 2.3 can be considered negligible for wavelengths of above 1.24 μm [30].

2.2 Software for Electrical Simulation

We used the device simulator SILVACO ATLAS^{TM} [31] for solving the poisson and the drift-diffusion equations to predict various internal characteristics in our modulator under various biased conditions for DC and transient analysis. These internal characteristics include electron and hole distribution, conduction band and valence band energies, electric field distribution,

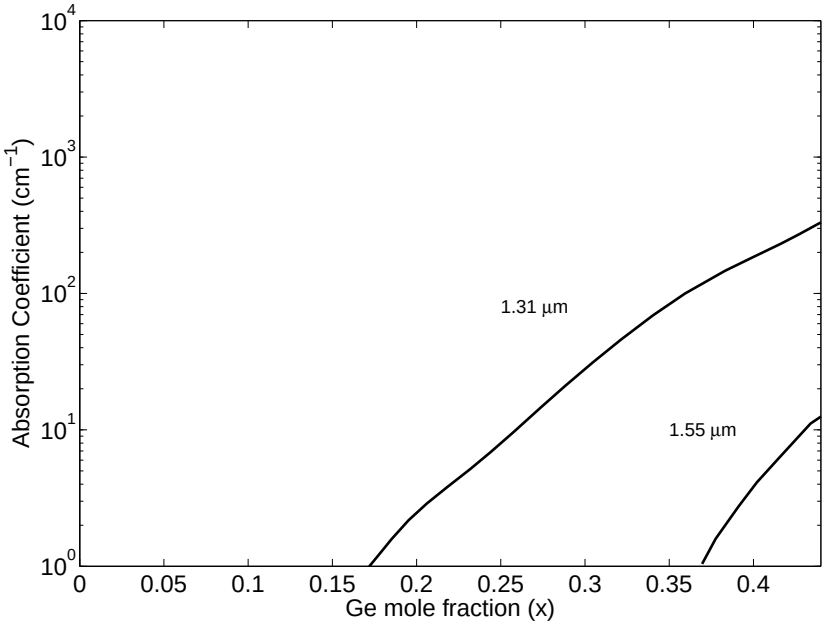

Figure 2.3: Absorption coefficient of Si and strained SiGe, temperature is 300K

etc. In section 2.2.1, we describe key components we need to define in the software before simulating a structure. In section 2.2.2, the models we used in the simulations of SiGe/Si quantum-well optical modulators are described.

2.2.1 Basic Steps of Electrical Analysis in ATLAS

Simulation of a device in SILVACO ATLAS^{TM} for the prediction of the internal behavior follows the following procedure. At first, the user has to define the structure by defining the thickness, the material composition and the doping profile of every layer of the structure. A mesh is defined for solving the various equations. The mesh is basically used to determine the nodes

at which various equations will be solved. A good practice is to define a fine mesh in regions where the device characteristics are of particular interest (quantum-wells in our modulator). The user then defines the various models for material parameters that are used in the simulation. The user then specifies the bias conditions for performing the electrical simulation. After the completion of the simulation, the device characteristics can be viewed using TONYPLOT (Graphical user interface) or these can be extracted as numerical data.

2.2.2 Models Incorporated for Device Simulation

In this section, we briefly discuss the models that we used in the modeling of our SiGe/Si modulator. Details of these models are found in the ATLAS manual [31].

2.2.2.1 Recombination Models

Shockley-Read-Hall (SRH) Recombination - Concentration dependent SRH model (CONSRH) is one of the recommended recombination models for Si and Si-based materials. Under the SRH recombination, recombination of excess carriers in a heavily doped semiconductor occur in the presence of a trap, which is an energy level within the forbidden gap of the semiconductor corresponding to a crystal impurity or vacancy, which alternately captures electrons and holes, as shown in Fig. 2.4. The rate of recombination depends on the lifetime of the excess carriers. In the case of the concentration dependent SRH model, the constant carrier lifetimes of electrons and holes will be functions of the impurity concentrations.

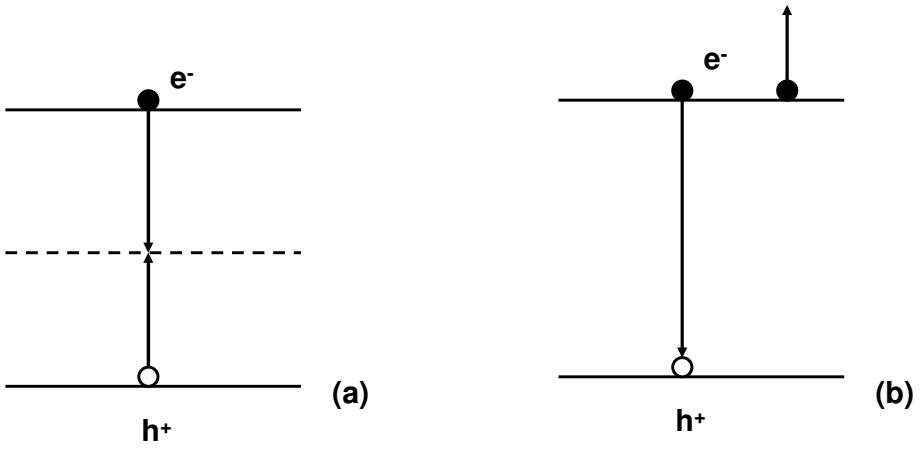

Figure 2.4: The two major recombination processes in silicon are (a) SRH recombination (b) Auger recombination

Auger Recombination - Under Auger recombination, electrons and holes recombine by a band-to-band transition and due to the recombination, a third carrier (electron or hole) is emitted.

As the Auger recombination is a 3 particle process, it is unlikely under low-level injection and therefore the SRH recombination dominates the recombination processes [32]. However, Auger dominates as the carrier density increases.

2.2.2.2 Mobility Models

To model the mobilities of holes and electrons in Si and SiGe layers, we used concentration dependent mobility (CONMOB) and electric field dependent mobility (FLDMOB) models.

The mobility of the carriers decrease with the increase of the doping con-

centration, as the ionized impurities introduced by the dopants will enhance the scattering process. That is why we used the CONMOB model.

The drift velocity of the carriers is the product of the mobility and the electric field in the direction of the current flow. The carrier velocity increases with the increase of the electric field. At high electric field, carriers that gain energy take part in a wider range of scattering process and there will be a reduction in the mobility of the carriers. Hence the velocity cannot increase much with the increase of electric field. Eventually, the velocity saturates at a constant velocity. To consider the effects of this saturation velocity, we used the FLDMOB model. We will see later in section 2.5 and 2.6 that this model does not have any effect on the internal characteristics of a device in the case of DC analysis, but it significantly affects the transient analysis.

2.2.2.3 Bandgap Narrowing Model

In the presence of heavy doping (greater than 10^{18} cm^{-3}), the bandgap of a semiconductor becomes doping dependent. As the doping level increases, a decrease in the bandgap separation occurs, where the conduction band is lowered by approximately the same amount as the valence band is raised. Details of this model can be found in the ATLAS manual.

2.2.2.4 Thermionic Emission and Tunneling

The thermionic field emission model takes into account the thermionic emission process at the abrupt heterojunction interface as well as the tunneling across the heterojunction. The band diagram of an abrupt heterojunction is

shown in Fig. 2.5. Electron transport across the conduction band spike can be described by tunneling through the spike and thermionic emission over it [33, 34].

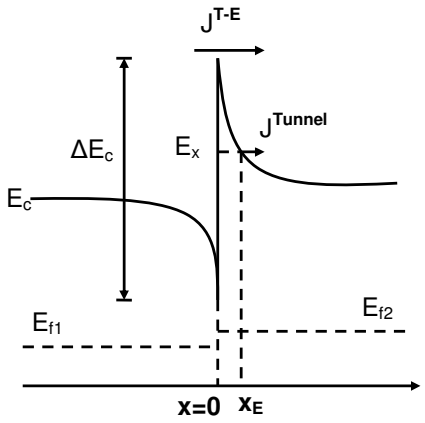

Figure 2.5: Schematic band diagram of an abrupt heterojunction. E_{f1} and E_{f2} represents the electron quasi-fermi level in each semiconductor region. J^{T_E} and J^{Tunnel} are the thermionic emission and tunneling current, respectively.

In a quantum-well, suppose the barriers to the right and to the left of the well are given by E_r E_l, respectively. A carrier of charge e and effective mass m^* must be higher in energy than one of the barriers in order to be able to leave the well. By applying an electric field across the well, the confined carrier concentration in the quantum-well will decrease as

$$\frac{\delta n(t)}{\delta t} = -\frac{n_0}{\tau_e} \tag{2.4}$$

where n_0 is the initial confined hole concentration and τ_e is escape characteristic time given by the thermionic and tunneling escape times $1/\tau_e =$

$1/\tau_{th}+1/\tau_{tun}$ [35]. The carrier population n of the well decays by thermionic emission with the time constant τ_{th} which is given by [35]

$$\frac{1}{\tau_h} = \frac{1}{w}\left(\frac{k_B T}{2\pi m^*}\right)^{\frac{1}{2}} \cdot exp\left(-\frac{E_{r,l} - E_i - qF\frac{w}{2}}{k_B T}\right) \tag{2.5}$$

where w is the barrier width, E_i is the energy of the carrier, and F is the applied electric field to the quantum-well. If no field is applied to the quantum-well, the thermionic emission and tunneling escape time will be very large and the carriers will not decay at zero electric field. When electric field is applied to the quantum-well, the thermionic emission time will decrease and the carriers can escape the quantum-well.

2.3 Optical Simulations

Section 2.3.1 describes the operating principle of a simple SOI planar waveguide (2-dimensional waveguide). Then four possible configurations of 3-dimensional waveguides are shown. A single mode SOI rib waveguide fabricated by Lardenois *et al.* [36] is discussed next. In section 2.3.2 we simulated the SOI rib waveguide described in [36] with a MATLAB mode solver and found that the SOI rib waveguide is single mode with a very low leakage loss.

2.3.1 Silicon-On-Insulator (SOI) Waveguides

A dielectric waveguide is formed when a high refractive index region is surrounded by regions of lower refractive index. Light propagating through the waveguide will be primarily confined to the high refractive index region

due to the total internal reflection at the boundaries between the higher and lower refractive index regions [37]. A simple SOI waveguide, shown in Fig. 2.6, consists of a silion layer (the higher refractive index material or core) sandwiched between a silica (SiO_2) layer and air (the lower refractive index materials). The SiO_2 layer (the lower cladding layer) should be thick enough to prevent light leaking into the silicon substrate.

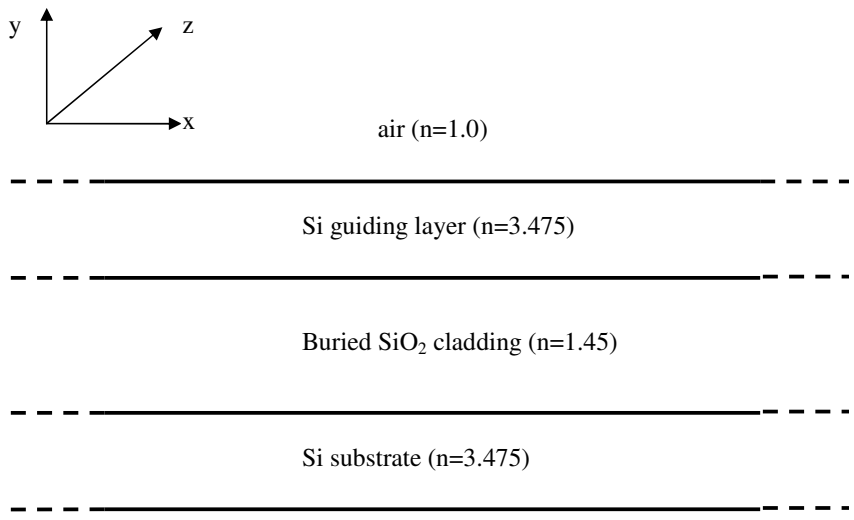

Figure 2.6: SOI planar waveguide, the refractive indices (n) of the layers are shown for the wavelength of 1.55 μm. The z direction is taken as the direction of light propagation.

The planar two-dimensional waveguide is useful for describing the theory of waveguides and the solution of Maxwells equations. But it confines the light only in one dimension (here the y direction in Fig. 2.6). For many

applications, two-dimensional confinement is required. There are several configurations used for three-dimensional waveguides, schematically represented in Fig. 2.7: strip (a), embedded strip (b), rib (or ridge) (c) and strip-loaded (d) waveguides. In SOI-based devices, the rib waveguide is most commonly used [32].

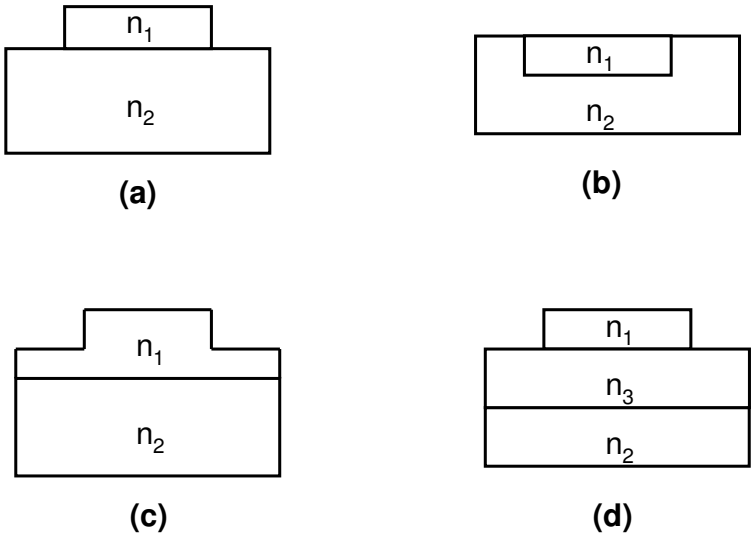

Figure 2.7: Different configurations of three dimensional waveguides (a) strip, (b) embedded strip, (c) rib (or ridge), and (d) strip-loaded waveguides.

Lardenois *et al*. (in the same group of Marris-Morini) fabricated a SOI rib waveguide [36]. The cross section of this waveguide is shown in Fig. 2.8. The buried SiO_2 thickness of the SOI waveguide was 700 nm, which is large enough to prevent lightwave from leaking towards the Si substrate. The Si film thickness was 400 nm which was reduced to 380 nm during the etching process. The etched depth of this waveguide was 70 nm. The rib

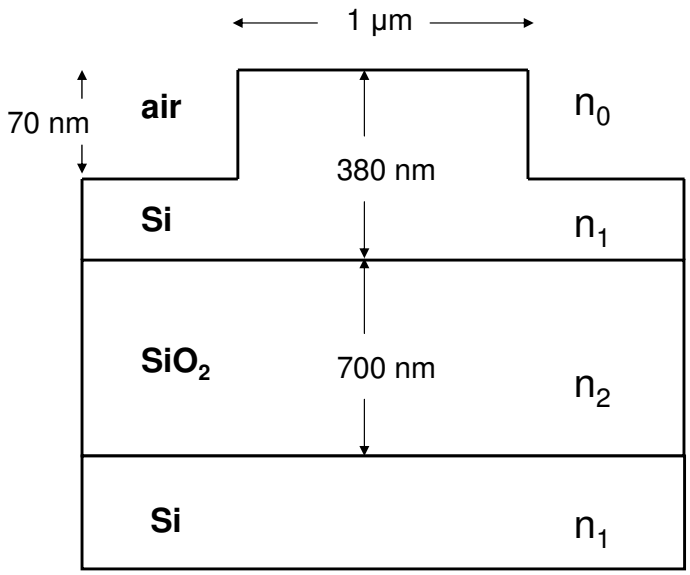

Figure 2.8: Cross section of the SOI rib waveguide discussed in [36].

width was 1 μm, which is close to the maximum value to ensure single mode conditions [36]. The measured propagation losses in this Si-SiO_2 rib waveguide was found to be 0.4 dB/cm. We simulated this SOI rib waveguide in the MATLAB mode solver program available online [38, 39]. In the next section, The simulation results (effective index and optical loss) obtained for the SOI rib waveguide is presented.

2.3.2 Mode Solver for Optical Simulation

The mode solver program [38] that we used for the simulation of the SiGe/Si waveguide modulator is described very briefly in Appendix B. Before sim-

ulating the SiGe/Si waveguide modulator with this program, we solved the eigenmodes of the SOI rib waveguide described in section 2.3.1. We defined the refractive index and the thickness of various layers of the SOI waveguide; the grid spacings both in x and y directions and an initial guess for the effective index of the TE_0 mode in the program. Now, as the refractive index profile is symmetric about the y axis, only half of the waveguide needs to be included in the computational domain. So we defined half of the rib width in the program. Then we defined the boundary conditions which are considered for the points on the edge of the computation window as described in Appendix B. The absorbing boundary condition is used for north (upper), south (lower) and east (right) boundary and the symmetric boundary condition is used for the west (left) boundary. Then we simulated the SOI waveguide described in section 2.3.1 for operation at 1.55 μm. We found that this waveguide is single mode and the modal effective index of the fundamental mode for TE polarization was $n_{eff} = 3.1193 + i1.792 \cdot 10^{-8}$. The mode profile is shown in Fig. 2.9.

2.4 Design of the SiGe/Si Optical Modulator

Marris *et al.* designed a 3 quantum-well modulator for operation at $\lambda_0 = 1.31$ μm using coupled electrical-optical simulations in Ref. [40]. In this paper, they provided all the device parameters as well as a figure on the depletion process of the holes with the application of reverse bias voltage showing the position of all of the layers. We extracted the thicknesses of the P^+ and N^+ layers and the NID layers next to these P^+ and N^+ layers from this figure.

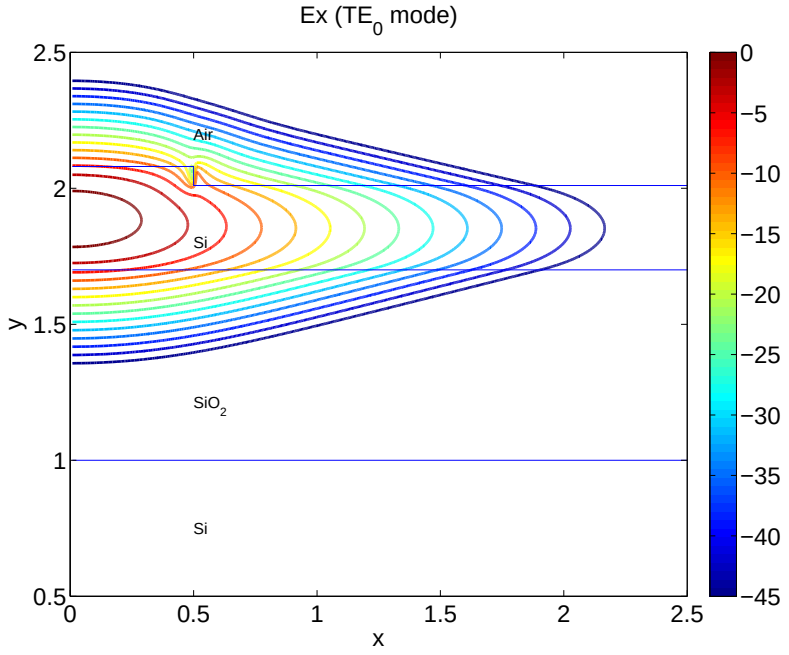

Figure 2.9: 2D Mode profile for the fundamental TE mode of the SOI rib waveguide discussed in [36]. Each line represents an identical field value (−3 dB step between lines, −45 dB minimum value).

In section 2.4.1, we describe the general structure of these modulators. The coupled electrical-optical analysis used to design these modulators is described in section 2.4.2. We performed the electrical analysis in two different modes: DC analysis and transient analysis. We performed the DC analysis in order to investigate the electrical and optical behaviors of the device with the application of various reverse bias voltages. For this analysis we varied the applied reverse voltage from 0 V to 10 V. Then we performed the transient analysis in order to investigate the frequency response of the device. For this analysis, at first a reverse bias voltage step from 0 to x V

(where $x = 6$ for the 3 quantum-well modulator) with a rise time of 1 fs was applied to the device and the electrical and optical behaviors of the device were observed at several times ranging from 0 to 100 ps. Then, a reverse bias voltage step from x to 0 V with a fall time of 1 fs was applied to the device and the electrical and optical behaviors of the device were observed at several times for the next 100 ps.

2.4.1 Device Structure

The modulator consists of a PIN (P-Intrinsic-N) diode; the active region consists of 'k' periodic stacks of layers (where $k = 3$ for the 3 quantum-well modulator). Each period consists of a 10 nm $Si_{0.8}Ge_{0.2}$ quantum-well surrounded by 10 nm Si-NID (Non-Intentionally Doped-10^{16} cm^{-3}) layers and 5 nm P^+ highly doped (2×10^{18} cm^{-3}) layers (P^+-δ-doped layers). The thickness of both of the P and N part of the PIN diode is 30 nm. The PIN diode (thickness t) is grown on a 30 nm Si-NID layer at the bottom of the PIN diode [26]. This structure is simulated using a 700 nm SiO_2 layer, which is thick enough to prevent the light leaking towards the Si substrate [36]. For the lateral confinement of light, a rib structure is defined, simulating the partial etching of the upper layers. The dimensions of the rib structure are defined such that this modulator could be integrated with a single mode SOI rib waveguide [36]. We discussed about this single mode SOI rib waveguide fabricated by Marris *et al.* in section 2.3.2. The mole fraction of Ge was chosen to be 0.2 to keep the bandgap of SiGe higher than the energy of the incident light to avoid band-to-band absorption and to maintain the total thickness below the critical thickness, as we described in section 2.1.1.

2.4.2 Electrical and Optical Analysis

With no field applied holes from the P^+ layers are captured by and confined in the quantum-wells and when a reverse bias is applied holes are released from the quantum wells and drift to the 30 nm P^+ contact layer. Variation of the hole distribution leads to a free-carrier absorption change and a refractive index change in each layer and, subsequently, the phase modulation of the guided optical wave. We calculated the hole distribution in the various layers of the structure using Silvaco ATLAS^{TM} [31]. The solution of Poisson-Fermi-Schroedinger equations is needed for the calculation of the hole density in the quantum-wells of the SiGe/Si modulator [41]. However, it was shown by Marris *et al.* (in Ref. [40]) that, if the quantum-well is equal to or thicker than 10 nm, the hole density profile in the structure at $V = 0$ V obtained by solving the Poisson-Fermi-Schroedinger equations is similar to that obtained by solving the Poisson-Fermi equations. That is why we used the Poisson-Fermi solver in Silvaco ATLAS^{TM} for the calculation of the hole density distribution at various applied voltages. The carrier transport in bulk material and at heterojunctions is calculated, respectively, using the drift-diffusion expressions and thermionic emission expressions [33, 34]. The models used by Marris *et al.* are the concentration dependent SRH (Shockley-Read-Hall) recombination model, the concentration dependent mobility model, the Auger model, and the Fermi-Dirac statistics model [40]. We used these models as well as two additional models: the field dependent mobility model and the band gap narrowing model. These additional models do not affect the DC analysis, but the field dependent

mobility model affects the transient analysis as described in section 2.6. Experimental results showed that the higher reverse bias voltages lead to higher reverse leakage currents, and, therefore, higher leakage power that might create a self heating of the device which, in turn, affects the effective index variation [42]. This thermo-optical index variation becomes more significant at higher reverse bias voltages. However, as well as Marris *et al.*, we ignored these effects in our calculations. The material parameters used for this simulation are the default parameters for Si and $Si_{0.8}Ge_{0.2}$ used in Silvaco ATLAS^{TM}. We tuned the bandgaps of these materials to be $E_{G-Si} = 1.12$ eV and $E_{G-Si_{0.8}Ge_{0.2}} = 0.972$ eV as defined in Ref. [26] and also the electron affinities to be $\chi_{Si} = 4.05$ eV and $\chi_{Si_{0.8}Ge_{0.2}} = 4.04$ eV [43].

The hole concentration obtained using the electrical simulation in Silvaco ATLAS^{TM} is averaged in each layer [44]. As the layers are very thin, this approximation gives a refractive index profile similar to the refractive index profile obtained using the actual hole concentration profile.

The absorption coefficient variation and refractive index variation in the doped Si layers with respect to undoped Si at $\lambda_0 = 1.55$ μm, is calculated from the hole distribution using the following formulae [23]

$$\Delta\alpha = 8.5 \times 10^{-18}\Delta N + 6.0 \times 10^{-18}\Delta P \tag{2.6}$$

$$\Delta n = -8.8 \times 10^{-22}\Delta N - 8.5 \times 10^{-18}\Delta P^{0.8} \tag{2.7}$$

where ΔN and ΔP are, respectively, the electron and the hole concentration variations cm^{-3} with respect to the intrinsic carrier concentration of every

layer.

To calculate the absorption coefficient change and the refractive index change in $Si_{0.8}Ge_{0.2}$ we used equation 2.6 and 2.7 due to the unavailability of separate equations for free carrier absorption for $Si_{0.8}Ge_{0.2}$ [35]. The intrinsic hole concentration of Si and $Si_{0.8}Ge_{0.2}$ are, respectively, taken as 0.668×10^{10} cm^{-3} and 10×10^{10} cm^{-3}, as defined in Silvaco ATLAS^{TM} at $T = 300^{o}$K. The refractive index of undoped Si and $Si_{0.8}Ge_{0.2}$ are taken as 3.475 and 3.505, respectively, for $\lambda_0 = 1.55$ μm. The absorption coefficient for undoped Si and $Si_{0.8}Ge_{0.2}$ are considered to be negligible at $\lambda_0 = 1.55$ μm.

The free carrier absorption as well as the refractive index of each layer are used as the input to a mode solver [38], which provides the effective index as well as the optical loss for TE polarized light at various voltages using a 2D semi-vectorial finite-difference approach. The optical loss can be converted into dB/cm using the formula $\alpha = 10 \cdot log_{10}e \times \frac{4\pi}{\lambda_0} \times N_i$ dB/cm, where N_i is the imaginary part of the effective index calculated in the mode solver.

2.5 DC analysis in 3 Quantum-Well SiGe/Si Modulator

A schematic diagram of the 3 quantum-well SiGe/Si modulator is shown in Fig. 2.10.

We re-analyzed this structure for operation at $\lambda_0 = 1.31$ μm. For a $V = 0$ V to $V = 6$ V variation Marris *et al.* obtained the effective index

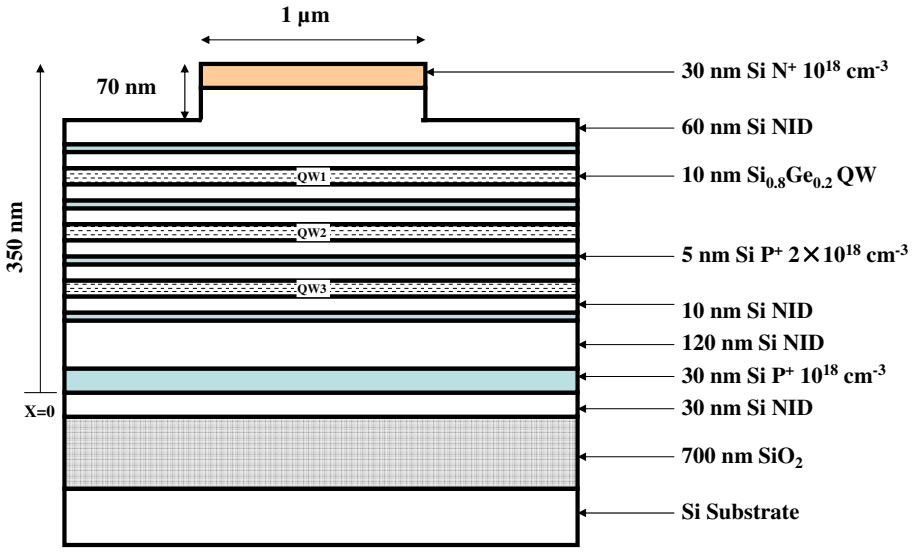

Figure 2.10: Schematic view of the 3 quantum-well SiGe/Si optical modulator.

variation of $1.7 \cdot 10^{-4}$. For a $V = 0$ V to $V = 6$ V variation, we obtained an effective index variation of $1.65 \cdot 10^{-4}$. Our result (effective index variation at $V = 6$ V) was consistent with their result. We, then, repeated the analysis for this structure for the wavelength of $\lambda_0 = 1.55$ µm, which gives a much lower $V_\pi L_\pi$ compared to the $V_\pi L_\pi$ obtained for the wavelength of $\lambda_0 = 1.31$ µm, the reasons will be discussed in section 2.5.2.

In section 2.5.1, various device internal characteristics such as the electron and hole distribution, conduction band and valence band energies, electric field distribution, etc., of the 3 quantum-well SiGe/Si optical modulator under various reverse bias voltages are discussed. Then, in section 2.5.2 we describe the absorption coefficient and the refractive index calculations using the hole distribution in various layers of the 3 quantum-well structure. The

absorption coefficient as well as the refractive index of each layer are used as an input in the mode solver we discussed in section 2.3.2, which provides the effective index as well as the optical loss. The effective index and optical loss calculation for the fundamental TE mode for operation at 1.31 and 1.55 μm using the mode solver program are presented in section 2.5.3. This section concludes with a comparison of the important performance characteristics (effective index variation and optical loss) for 1.31 and 1.55 μm.

2.5.1 Electrical Analysis

For the DC analysis, we applied reverse bias voltages ranging from 0 V to 10 V to this modulator. The hole distribution in the structure is calculated using Silvaco ATLAS^{TM} at each applied reverse bias voltage. The hole concentrations for the 3 quantum-well structure at several specific voltages are shown in Fig. 2.11.

With no field applied, holes from the P^+ layers are captured by and confined in the quantum-wells and when a reverse bias is applied, holes are released from the quantum wells and drift to the 30 nm P^+ contact layer. The band profiles and the electric field profiles in the structure at $V = 0$ V and at $V = 6$ V are shown respectively in Fig. 2.12(a) and Fig. 2.12(b). It can be seen that at $V = 6$ V, the valence band in the first two quantum-wells are fully bent and only partially bent in the 3rd quantum-well. In other words, the first two quantum-wells are fully depleted and the 3rd quantum-well is almost depleted for $V = 6$ V. Fig. 2.12(b) shows that inside the quantum-wells, the slope of the electric field is positive at $V = 0$ V due to the confinement of holes. With the application of a reverse bias, holes are

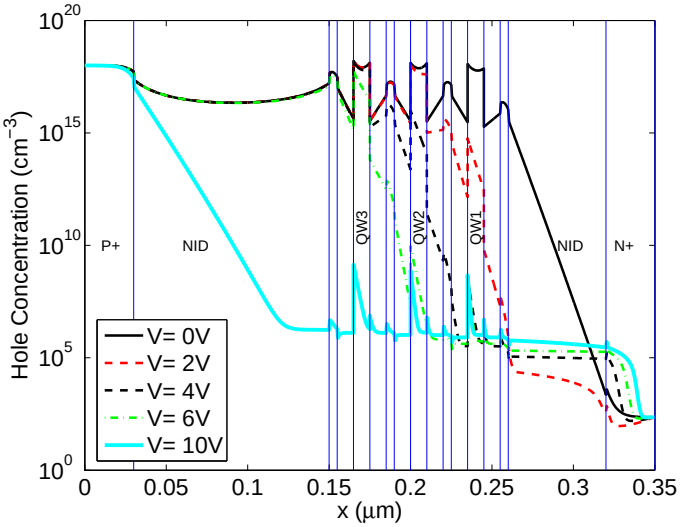

Figure 2.11: Hole distribution in various layers at various reverse bias voltages. With the increase of reverse biasing, hole deplete from the quantum-wells. Holes starts to deplete from the NID layer on the P^+ side after all the quantum-wells are fully depleted i.e. after 7.5 V NID layer starts depleting.

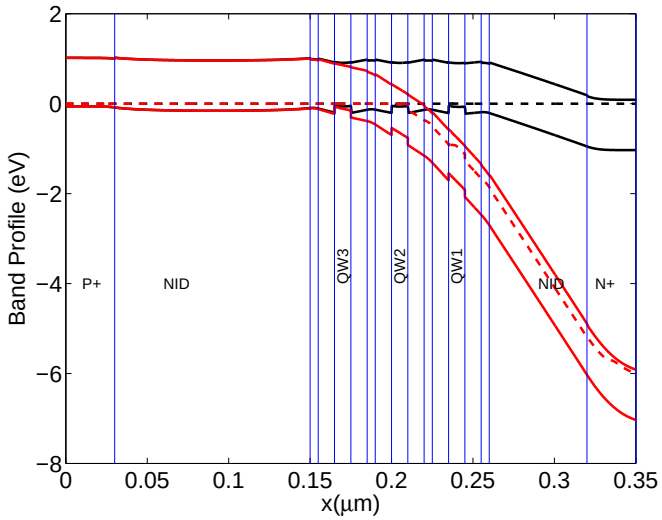

(a)

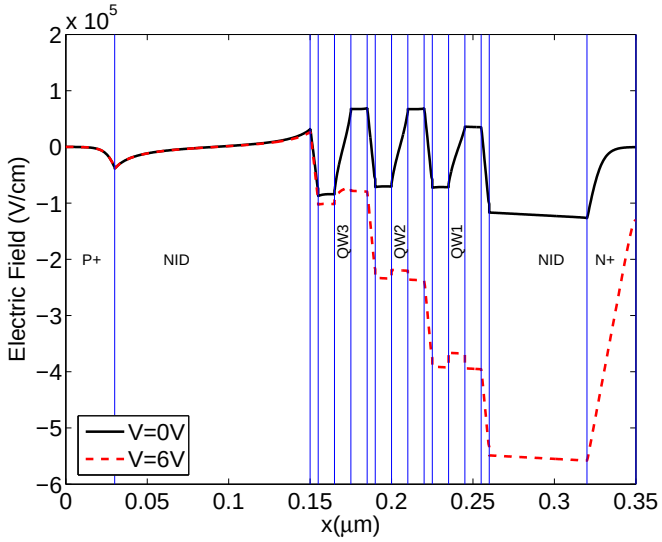

(b)

Figure 2.12: (a) Valence and conduction band energy profiles for the 3 quantum-well SiGe/Si structure, black lines are for $V = 0$ V and red lines are for $V = 6$ V, the dotted line shows the quasi-fermi energy level for holes (b) electric field in the 3 quantum-well SiGe/Si structure.

removed from the quantum-wells and the electric field is almost flat inside the quantum-wells at $V = 6$ V.

2.5.2 Calculation of Absorption Coefficient and Refractive Index

The hole concentration is averaged in each layer at each applied voltage [44]. As the layers are very thin, this approximation gives an effective index variation with applied reverse bias similar to the effective index variation obtained using the actual hole concentration profile as shown in Fig. 2.13.

The absorption coefficient variation and refractive index variation in the doped Si layers with respect to undoped Si at $\lambda_0 = 1.55$ μm is calculated from the hole distribution using equations 2.6 and 2.7.

In our calculations, we considered only the hole concentration change in the various layers, as the electron concentration is negligible with respect to the hole concentration except in the N^+ layer, where the electron concentration is relatively high as shown in Fig 2.14. For this N^+ layer, the refractive index and the absorption coefficient at $V = 0$ V is calculated from both ΔN and ΔP (ΔN is considered as the doping density of this layer).

Fig. 2.15(a) shows that the refractive index changes in the quantum-wells are much higher at $\lambda_0 = 1.55$ μm than at $\lambda_0 = 1.31$ μm which implies a higher effective index variation at $\lambda_0 = 1.55$ μm than at $\lambda_0 = 1.31$ μm. Fig. 2.15(a) shows that the refractive index change saturates with a saturation value of 1.6×10^{-3}, 1.95×10^{-3}, and 2.1×10^{-3} at 2.1 V, 4.3 V, and 7.5 V, respectively, in quantum-wells 1, 2, and 3, which indicates the quantum wells are depleted. Also, Fig. 2.15 (a) shows that the onset of the change

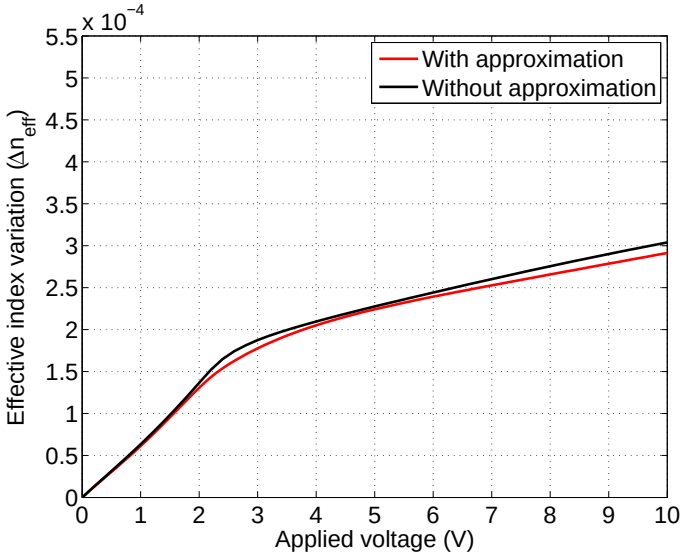

(a)

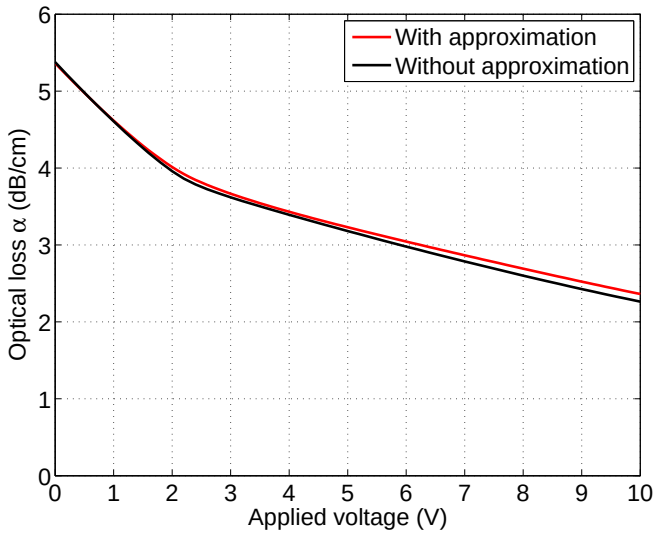

(b)

Figure 2.13: (a) Effective index variation in a single quantum-well modulator with and without averaging the hole concentration (b) optical loss with and without averaging the hole concentration.

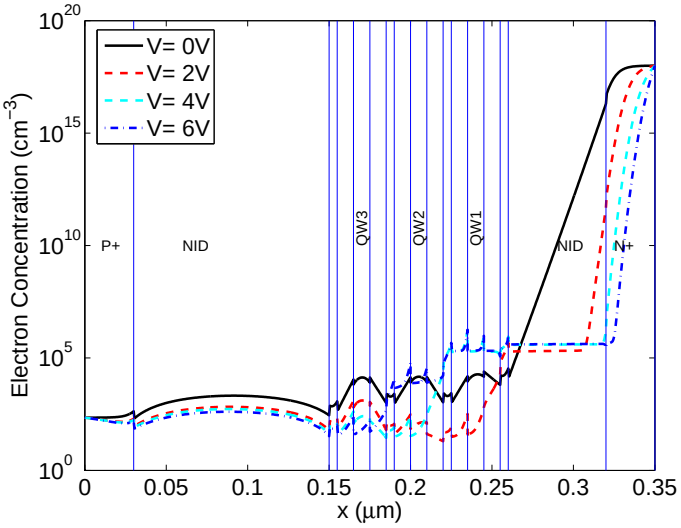

Figure 2.14: Electron distribution in various layers at various reverse bias voltages

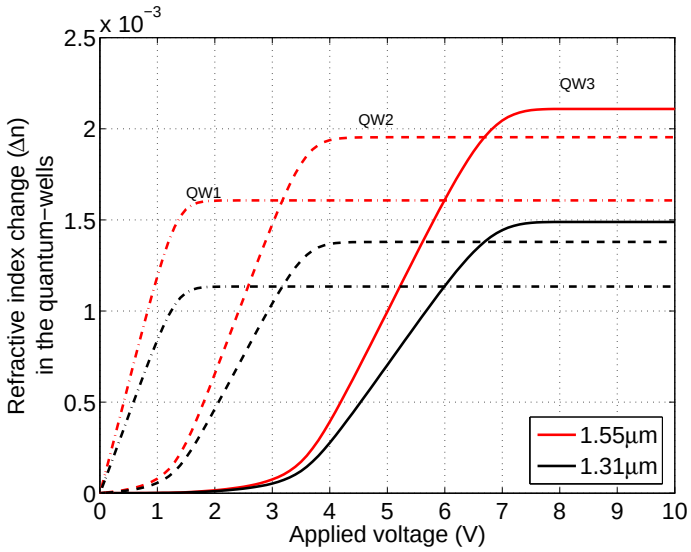

(a)

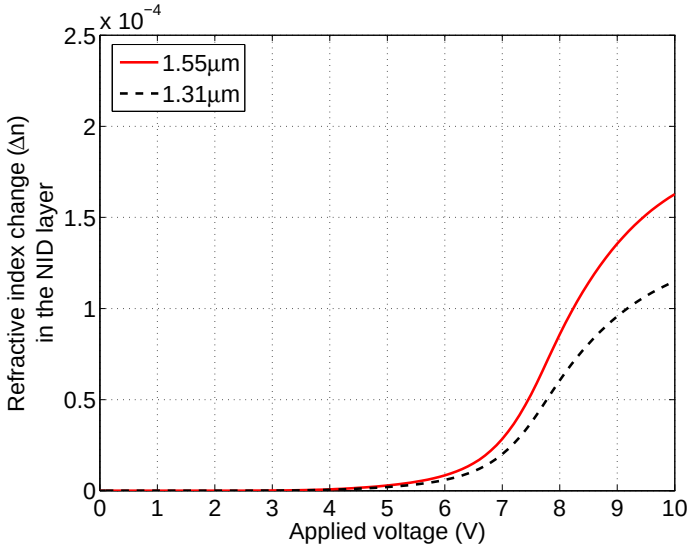

(b)

Figure 2.15: Refractive index changes ($\Delta n_v = n_v - n_0$) at $\lambda_0 = 1.55$ μm and $\lambda_0 = 1.31$ μm (a) in the quantum-wells with dash-dot line, dotted line, and solid line for quantum- well 1, 2, 3 respectively. (b) in the NID layer on the P^+ side

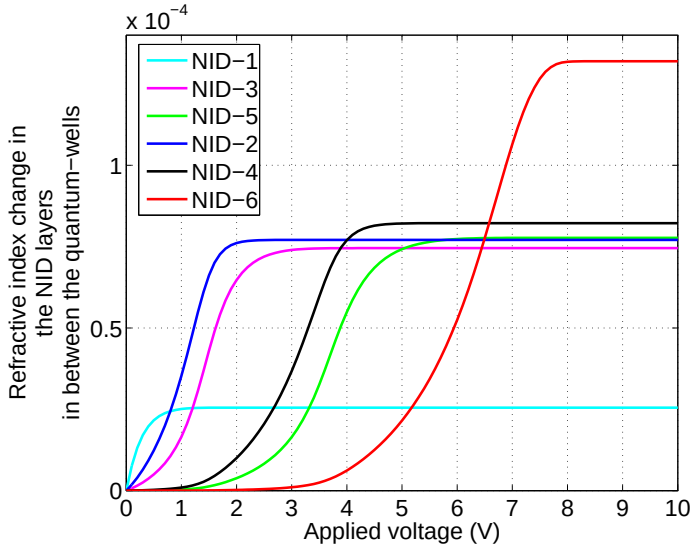

(a)

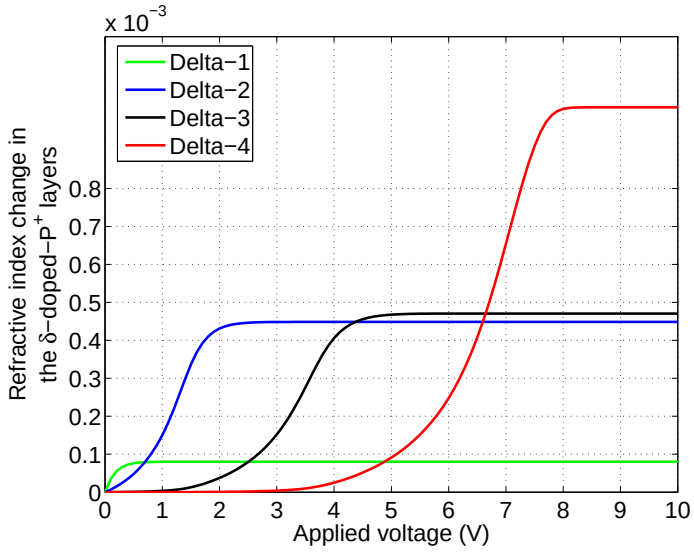

(b)

Figure 2.16: Refractive index changes at $\lambda_0 = 1.55$ μm in the (a) NID layers (b) δ-doped-P^+ layers

in refractive index in each of the quantum-wells occurs near the saturation value of the preceding quantum-well.

After the depletion of all 3 quantum-wells, the NID layer on the P^+ side starts depleting as well. Fig. 2.15(b) shows the refractive index changes in the NID layer on the P^+ side. The refractive index changes in the other layers (NID layers in between the quantum-wells and the P^+-δ-doped layers) are very small as shown in Fig. 2.16.

2.5.3 Effective Index and Optical Loss Calculation

The free carrier absorption as well as the refractive index of each layer are used as the input to a mode solver [38], which provides the effective index as well as the optical loss for TE polarized light at various voltages. The effective index variation curve for the 3 quantum-well structure is shown in Fig. 2.17(a). When the bias is lower than 7.5 V the effective index variation in the modulator is mainly caused by the refractive index change in the quantum-wells. Above 7.5 V, the refractive index changes in all of the quantum-wells become constant. However, above V=7.5 V the contribution from the NID layer on the P^+ side to the effective index variation becomes significant. In other words, after the depletion of all of the quantum-wells, the quantum-well modulator turns into a NID-layer modulator.

The two most important performance parameters obtained for this modulator are the effective index variation and optical loss which are found to be around 2.28×10^{-4} and 3.13 dB/cm at $V = 6$ V for the wavelength of $\lambda_0 = 1.55$ μm as shown in Fig. 2.17(a) and Fig. 2.17(b), respectively. To evaluate the modulation efficiency of the phase modulator, a figure of merit

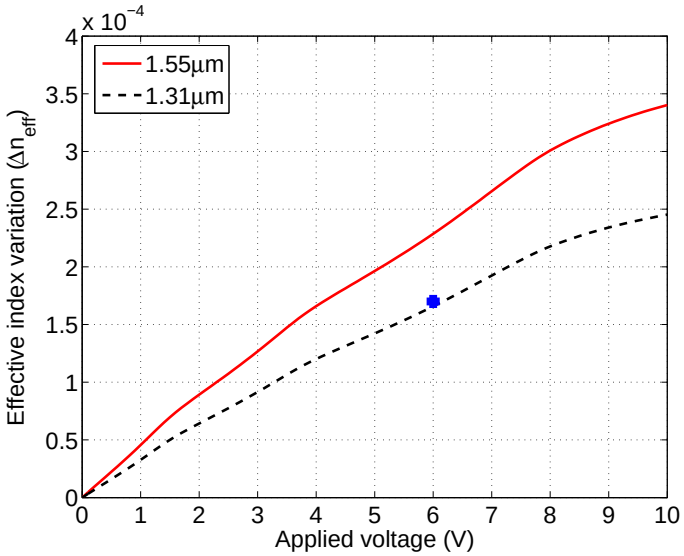

(a)

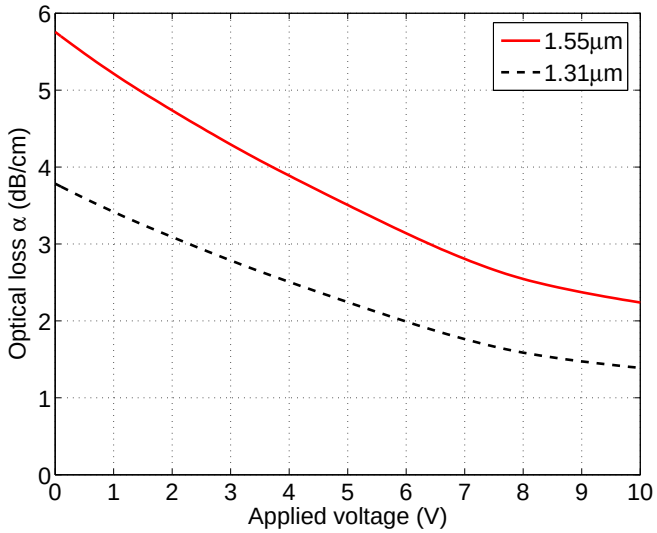

(b)

Figure 2.17: (a) Effective index variation ($\Delta n_{\text{eff-v}} = n_{\text{eff-v}} - n_{\text{eff-0}}$) of the 3 quantum-well modulator; the blue point shows the effective index variation at 6 V obtained by Marris *et al.* in Ref. [39] (b) optical loss at various voltages.

can be defined as the $V_\pi L_\pi$ product, where V_π and L_π are, respectively, the applied voltage and the length required to obtain a π phase shift of the guided wave. L_π can be calculated from the formula $L_\pi = \lambda_0/2\Delta n_{\text{eff}}$ where, Δn_{eff} is the effective index variation at the applied bias of V_π. The effective index variation of 2.28×10^{-4} at $V = 6$ V leads to a $V_\pi L_\pi$ of 2.039 V·cm ($L_\pi = 0.349$ cm) for the 3 quantum-well structure defined in [40] for $\lambda_0 = 1.55$ μm, which is much lower than the $V_\pi L_\pi$ of 2.37 V·cm obtained for $\lambda_0 = 1.31$ μm predicted by our analysis, at $V = 6$ V. The optical loss is slightly higher at $\lambda_0 = 1.55$ μm as compared to that at $\lambda_0 = 1.31$ μm, which is consistent with the experimental results [7].

2.6 Transient Analysis

Transient analysis is performed to evaluate the response time of the 3 quantum-well modulator $\lambda_0 = 1.55$ μm using thermionic emission, tunneling, and field dependent mobility model. Marris *et al*. did not use the field dependent mobility model while doing the transient simulations [40]. But we found that, in case of transient analysis, the field dependent mobility significantly affects the transient response. The drift velocity of the carriers is the product of the mobility and the electric field in the direction of the current flow. The carrier velocity will increase with the increase of the electric field but at high electric fields, it will begin to saturate due to the reduction of the effective mobility. Hence, without using the field dependent mobility model, the response would be much faster than when using this model and the modulation speed will be overestimated.

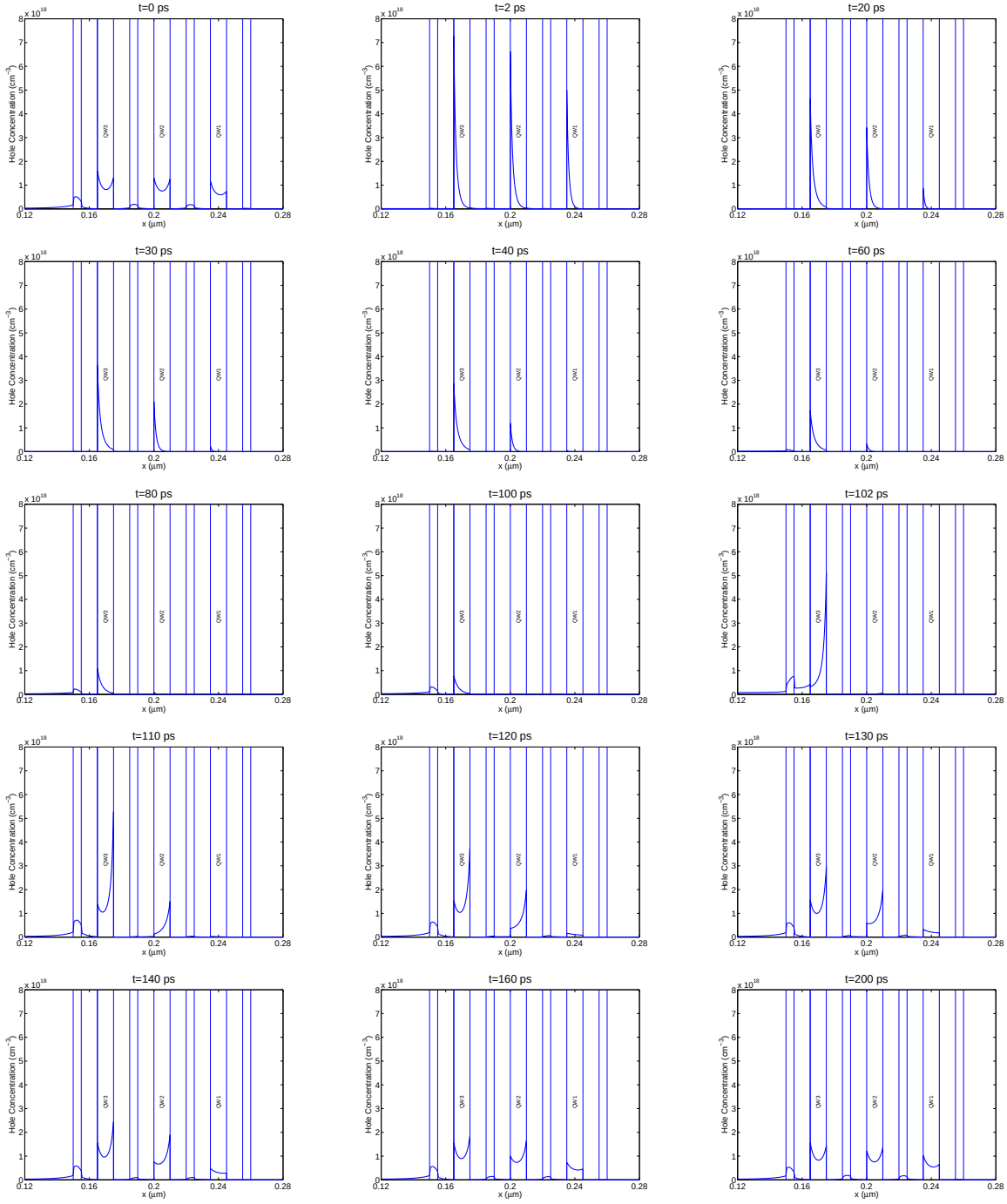

Figure 2.18: Hole density distribution at various times in the 3 quantum-well modulator, only the quantum-wells and the P^+ layers are shown in the figure.

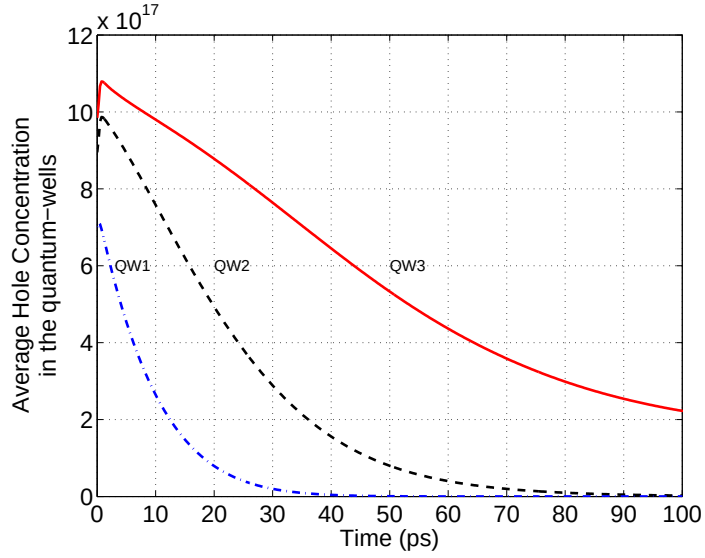

(a)

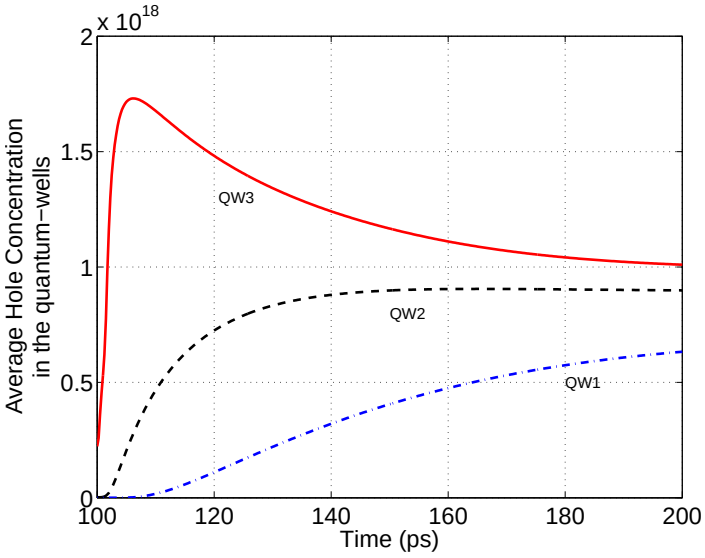

(b)

Figure 2.19: Hole density distribution with time in the 3 quantum-well modulator for (a) $t = 0$ ps to $t = 100$ ps (b) $t = 100$ ps to $t = 200$ ps.

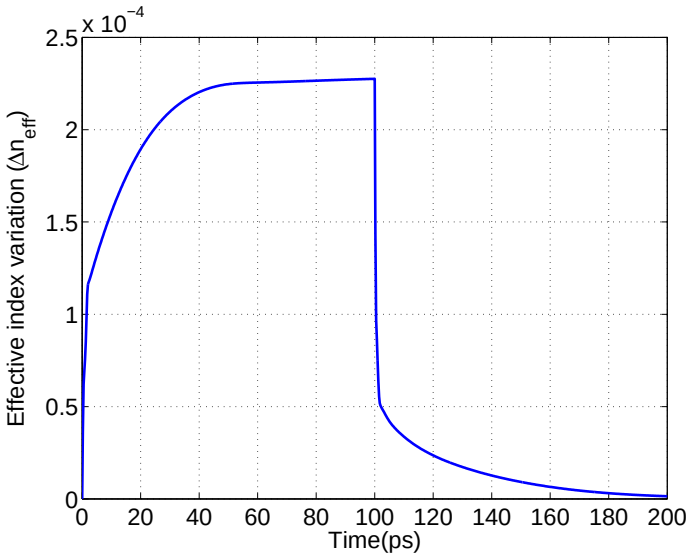

(a)

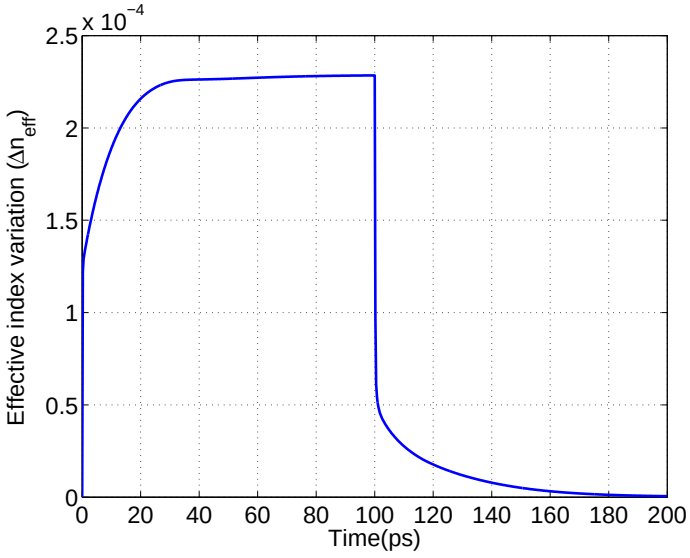

(b)

Figure 2.20: Effective index variation with time in the 3 quantum-well modulator for 0 to 6 V variation (a) with field dependent mobility model (b) without field dependent mobility model.

At first a reverse bias voltage step from 0 to 6 V, with a rise time of 1 fs, is applied to the device. The hole density distributions in the case of 3 quantum-well modulator obtained at several specific times during depleting the quantum-wells, are plotted in Fig. 2.18. The holes are initially confined in the three quantum-wells at $t = 0$. As time increases, initially the holes do not escape from the quantum-wells, they simply distribute themselves along the left side of each quantum-well. By $t = 36$ ps and $t = 80$ ps the 1st and the 2nd quantum-wells are depleted, respectively. By $t = 100$ ps, only a few holes are left in the 3rd quantum-well. Fig. 2.19(a) shows that the quantum-wells are depleting sequentially in time as described in Ref. [40].

After 100 ps, the applied voltage returned to zero with a fall time 1 fs. The hole density distributions obtained at several specific times, during which the holes are returning to the quantum-wells, are plotted in Fig. 2.18. Fig. 2.19(b) shows that at $t = 150$ ps, the average hole distribution became constant in the 3rd and 2nd quantum-well. The hole density distribution in the 1st quantum-well becomes constant after $t = 180$ ps.

In case of transient analysis, the field dependent mobility has significant effects on the effective index variation. The effective index variation curves with time with and without the FLDMOB are shown in Fig. 2.20(a) and Fig. 2.20(b) respectively. The initial sharp increase of effective index variation is due to the hole density change of the NID layer as the quantum-wells are not depleted initially.

2.7 Conclusion

In this chapter we found that, in the 3 quantum-well SiGe/Si structure, the quantum-wells deplete sequentially both with time and voltage. During the DC analysis, from Fig. 2.15(a), we found that the quantum-well 1, 2, and 3 are depleted at 2.1 V, 4.3 V, and 7.5 V, respectively. This figure also showed that below 1.5 V, the effective index variation Δn_{eff} is mainly caused by the refractive index change in the first quantum-well. The onset of the change in the refractive index in the second quantum-well occurs after the refractive index change in the first quantum-well approaches the saturation value. If we want to operate in a low bias region (below 1.5 V), only one quantum-well may be sufficient to have the same effective index variation as we obtained in the 3 quantum-well structure.

Again, during the transient analysis, from Fig. 2.19(a), we found that by $t = 36$ ps and $t = 80$ ps the 1st and the 2nd quantum-wells are depleted, respectively. By $t = 100$ ps, only a few holes are left in the 3rd quantum-well. If we can get rid of the last 2 quantum-wells, the hole depletion process from the quantum-well could be done by $t = 36$ ps.

Hence we removed 2 quantum-wells in the 3 quantum-well modulator and designed a single quantum-well modulator which will be discussed in the next chapter.

Chapter 3

Single Quantum-Well SiGe/Si Optical Modulator

In the 3 quantum-well structure, we found that when the voltage is lower than $V = 1.5$ V, the effective index variation Δn_{eff} is mainly caused by the refractive index change in the first quantum-well. The onset of the change in the refractive index in the second quantum-well occurs after the refractive index change in the first quantum-well approaches the saturation value. This implies that only one quantum-well may be needed to obtain the same effective index variation as is obtained in the 3 quantum-well structure for voltages below about $V = 1.5$ V. This single quantum-well structure can give the additional benefit of higher intrinsic speed over the 3 quantum-well modulator as we concluded from the results of the transient analysis of the 3 quantum-well modulator in chapter 2. Therefore we designed a single quantum-well modulator keeping the thicknesses and doping levels constant for all of the layers (*i.e.*, 2 QW layer stacks are removed).

The results obtained using the DC analysis for the single quantum-well modulator are described in section 3.1. The transient response for this modulator is described in section 3.2. The single quantum-well phase modulator

can be converted into an intensity modulator by inserting it into each of the arms of a Mach-Zehnder interferometer and by applying a bias voltage to each of the arms as described in section 1.3.1. The performance of such a Mach-Zehnder Interferometer is described in section 3.3.

3.1 DC analysis in Single Quantum-Well SiGe/Si Modulator

A schematic diagram of the single quantum-well SiGe/Si modulator is shown in Fig. 3.1.

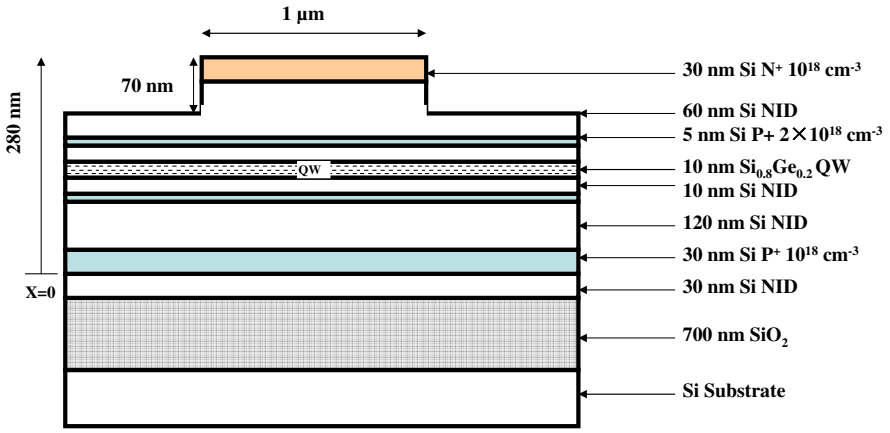

Figure 3.1: Schematic view of the SiGe/Si optical modulator.

For the DC analysis, we applied reverse bias voltages ranging from 0 V to 10 V to this modulator. The hole distribution in the structure is calculated using Silvaco ATLAS^{TM} at each applied reverse bias voltage. In section

3.1.1 we present the results of the refractive index calculations using the hole distribution in various layers of the single quantum-well modulator. The effective index and optical loss for the fundamental TE mode for operation at 1.55 μm are presented in section 3.1.2. Section 3.1.2 concludes with a comparison of the important performance characteristics (effective index variation, optical loss, and $V_\pi L_\pi$) for 3 quantum-well and single quantum-well modulator.

3.1.1 Refractive Index Change in Single SiGe/Si Quantum-Well Optical Modulator

The refractive index change in the single quantum-well saturates at about 2 V as shown in Fig. 3.2. The single quantum-well structure changes from a quantum-well modulator into a NID-layer modulator at this voltage due to the significant contribution of the refractive index change of the NID layer on the P^+ side as shown in Fig. 3.2.

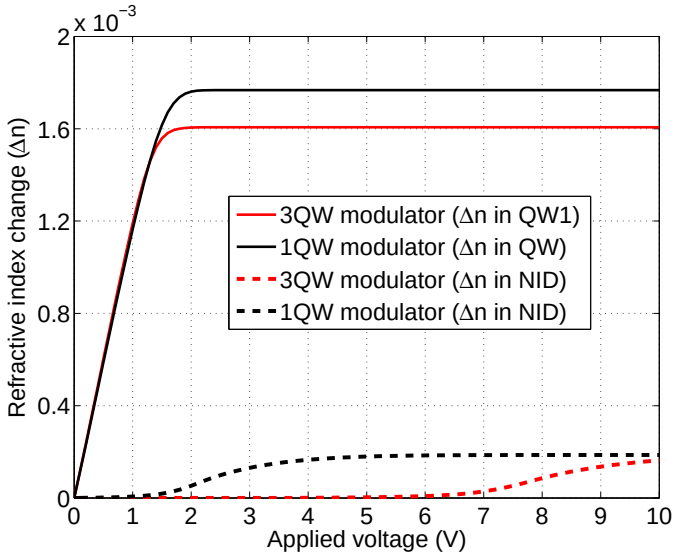

Figure 3.2: Comparison of the refractive index change in the single quantum-well structure and in the first quantum-well of the 3 quantum-well structure at $\lambda_0 = 1.55$ μm. The refractive index change in the NID layers on the P^+ side are shown for both the single quantum-well and the 3 quantum-well modulator.

3.1.2 Effective Index and Optical Loss Calculation

The effective index variation curves and their slopes are shown in Fig. 3.3. Fig. 3.3(a) illustrates that below 2 V the effective index variation in the single quantum-well structure is slightly higher than that in the 3 quantum-well structure. Above 2 V, and considering only the refractive index changes in the quantum-wells, the effective index variation in the single quantum-well structure becomes smaller than that in the 3 quantum-well structure as shown by the dotted line in Fig. 3.3(a). However, due to the onset of the refractive index change in the NID layer on the P^+ side, the single quantum-

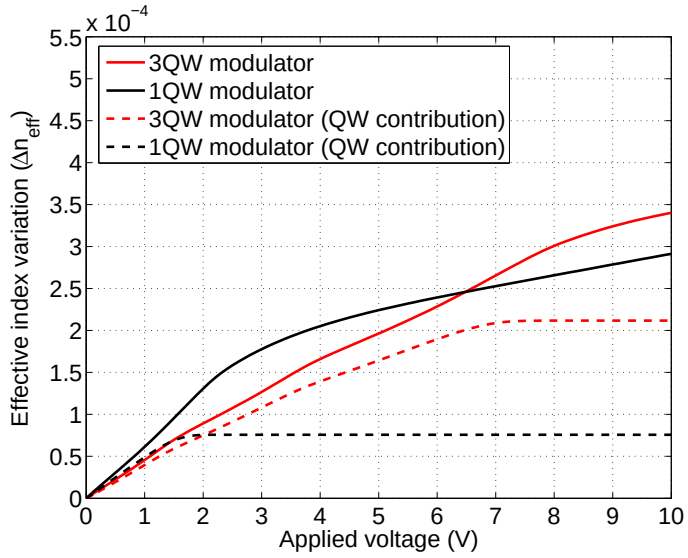

(a)

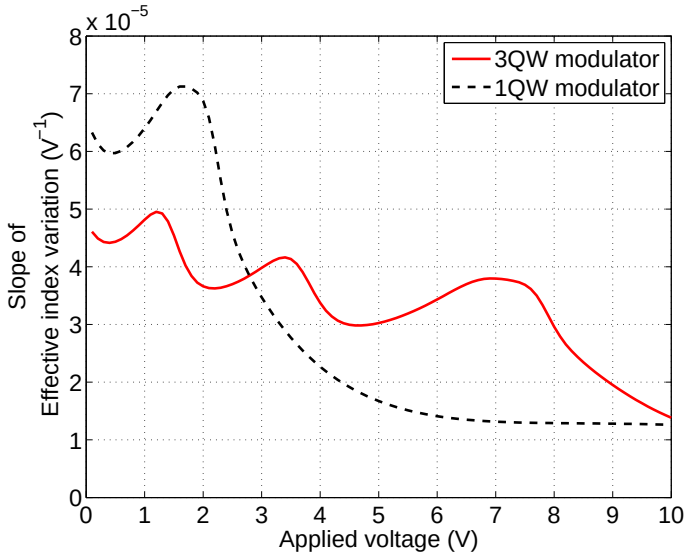

(b)

Figure 3.3: Comparison of the (a) effective index variation (b) slope of the effective index variation for single quantum-well and 3 quantum-well structure.

well structure shows significantly higher effective index variation than the 3 quantum-well structure until the cross-over point at about 6.5 V. Above 6.5 V, the 3 quantum-well modulator turns into a NID-layer modulator and the effective index variation in the 3 quantum-well structure becomes greater than that in the single quantum-well structure due to the combined effects of the refractive index changes in the quantum-wells and the NID layer. The optical loss in the single quantum-well structure is lower than that of the 3 quantum-well structure due to the removal of the two quantum-wells as well as the other doped layers. The optical losses for both of the structures are shown in Fig. 3.4.

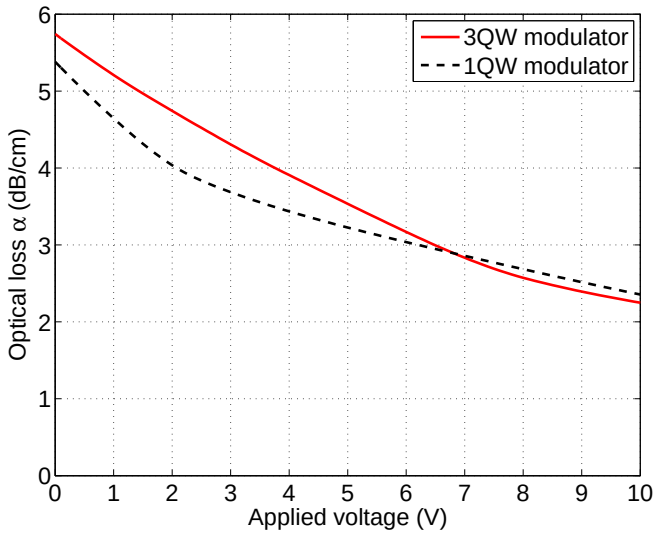

Figure 3.4: Comparison of the optical loss in the single quantum-well modulator and the 3 quantum-well modulator.

The highest slope of the effective index variation (0.71×10^{-4} V^{-1}) for the single quantum-well modulator occurs at about 1.6 V, as shown

in Fig. 3.3(b). At this voltage, the effective index variation with respect to 0 V is 1.02×10^{-4} . If we desire a V_π of 1.6 V for digital signal modulation, the $V_\pi L_\pi$ of this modulator will be 1.208 V·cm ($L_\pi = 0.759$ cm) which is much lower as compared to the $V_\pi L_\pi$ of the 3 quantum-well structure (2.039 V·cm) previously defined. For low voltage modulation, we can apply a voltage between 1.4 V and 1.8 V (*i.e.*, ±0.2 V about 1.6 V). Hence, if we desire a V_π of 0.4 V, for low voltage modulation, the $V_\pi L_\pi$ of this modulator will be 1.09 V·cm, which is also lower than the $V_\pi L_\pi$ of the 3 quantum-well modulator. The 3 quantum-well modulator that we studied in chapter 2 was optimized by Marris *et al.* to get the best performance in terms of the effective index variation and the optical loss by studying the influence of the thicknesses and doping levels of various layers in the structure. But we have not yet optimized the single quantum-well modulator. If we do the optimization of the single quantum-well modulator by doing such studies, it may give even lower $V_\pi L_\pi$ than that of the 3 quantum-well modulator.

3.2 Transient Analysis

In the case of the single quantum-well modulator, at first, a reverse bias voltage step from 0 to 1.6 V, with a rise time of 1 fs, is applied to the device. The hole density distributions obtained at several specific times, are plotted in Fig. 3.5.

Most of the holes are initially confined in the quantum-well at $t = 0$. Most of the holes are removed from the quantum-well by $t = 36$ ps. By $t =$ 100 ps, only a few holes are left in the quantum-well as shown in Fig. 3.6(a).

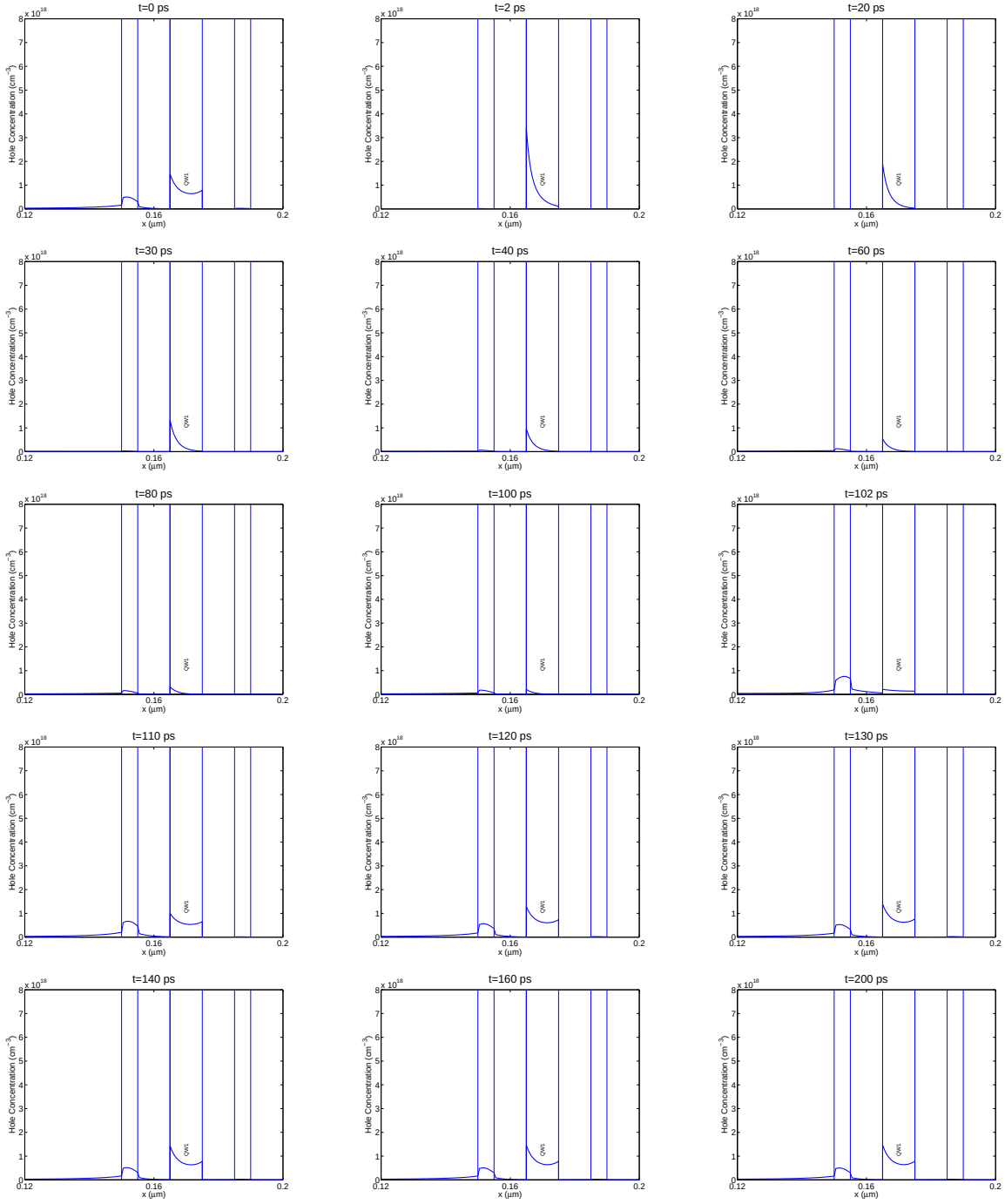

Figure 3.5: Hole density distribution at various times in the single quantum-well modulator, only the quantum-well and the P^+ layers are shown in the figure.

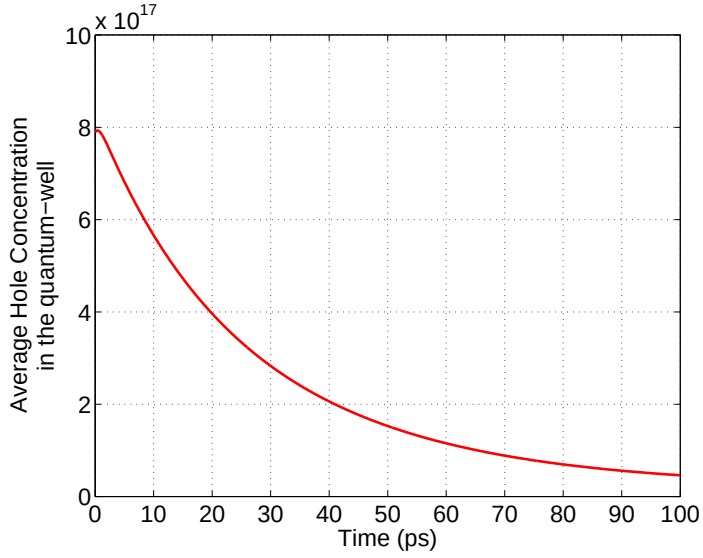

(a)

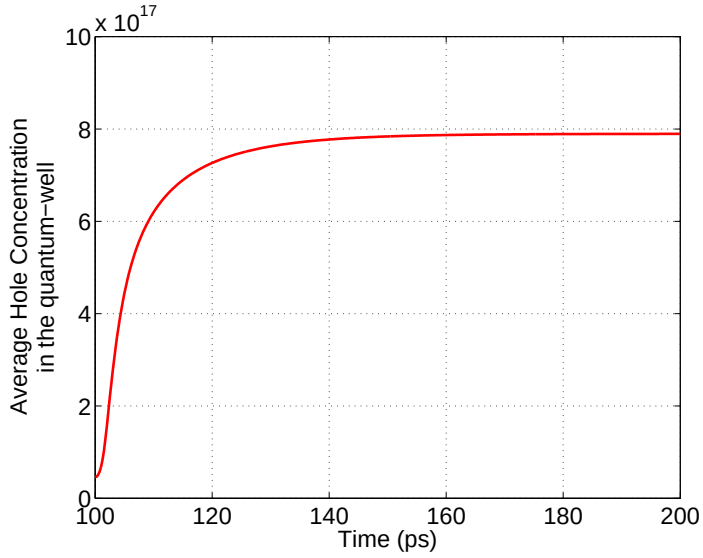

(b)

Figure 3.6: Hole density distribution with time in the single quantum-well modulator for (a) $t = 0$ ps to $t = 100$ ps (b) $t = 100$ ps to $t = 200$ ps.

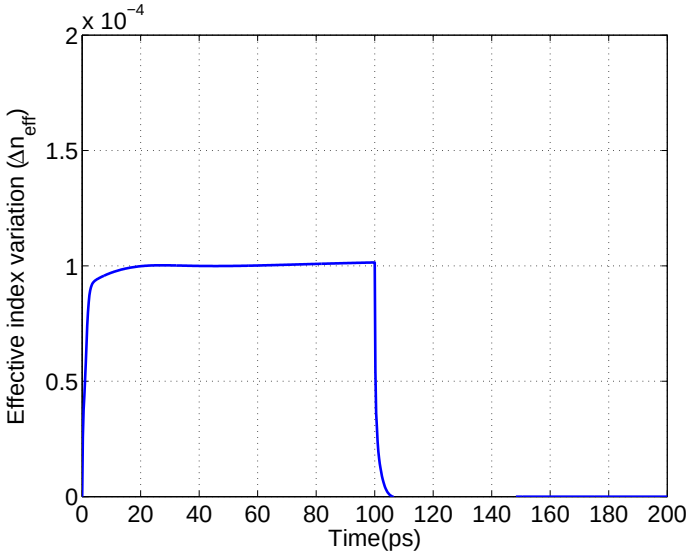

Figure 3.7: Effective index variation with time in the single quantum-well modulator for 0 to 1.6 V variation.

Hence, we can say that the hole depletion process is much faster in the case of the single quantum-well modulator than in the case of the 3 quantum-well modulator. After 100 ps, the applied voltage returns to zero with a fall time 1 fs. Fig. 3.6(b) shows that at $t = 140$ ps, the average hole distribution becomes constant in the quantum-well.

The effective index variation curve for the single quantum-well modulator is shown in Fig. 3.7. From this figure we can conclude that the transient response of the electro-optic effect in the single quantum-well modulator will be faster than that in the 3 quantum-well modulator. For the 3 quantum-well modulator the rise time (the time required for the effective index variation to increase from 10% to 90% of the maximum value) and the fall time (the time required for the effective index variation to decrease from 90% to 10% of the maximum value) are found to be around 26.6 ps and 21 ps, respectively. In case of the single quantum-well modulator these are found to be around 3.02 ps and 2.25 ps, respectively. Due to decrease of the time constants, the single quantum-well modulator will give higher intrinsic speed than the 3 quantum-well modulator.

3.3 Mach-Zehnder Interferometer Performance

The single quantum-well phase modulator can be converted into an intensity modulator by inserting it into each of the arms of the Mach-Zehnder interferometer and by applying a bias voltage to each of the arms as we described in section 1.3.1. Both the effective index variation (Δn_{eff} related to the modification of the propagation constants $\Delta\beta$) and the absorption

variation ($\Delta\alpha$) of the light beams, which are functions of the applied voltage to the phase shifters, will have effects on the output intensity of the Mach-Zehnder interferometer. Assuming identical waveguides, and assuming an ideal splitter and combiner, the Mach-Zehnder intensity transmission is given by (see appendix A):

$$\frac{I_{out}}{I_{in}}(V) = \frac{1}{4}\left[e^{-\alpha_1(V)L_1} + e^{-\alpha_2(V)L_2} + 2\cdot e^{-\alpha_1 L_1/2+\alpha_2 L_2/2}\cdot cos\left(\beta_2(V)L_2 - \beta_1(V)L_1\right)\right] \tag{3.1}$$

where L_1 and L_2 are the lengths of phase shifter 1 and phase shifter 2, respectively; β_1 and β_2 are the propagation constants of the light beams propagating through the phase shifters, and α_1 and α_2 are the propagation losses of the phase shifters. Assuming reverse bias are applied to both of the arms,

$$\beta_1 = \beta_0 + \Delta\beta_1 \tag{3.2}$$

$$\beta_2 = \beta_0 + \Delta\beta_2 \tag{3.3}$$

$$\alpha_1 = \alpha_0 - \Delta\alpha_1 \tag{3.4}$$

$$\alpha_2 = \alpha_0 - \Delta\alpha_2 \tag{3.5}$$

The length of the two phase shifters are taken to be $L_1 = 0.5$ cm and $L_2 = 0.7$ cm respectively. The voltage applied to the 0.5 cm branch is varied (modulating arm/arm 1) and the voltage at the 0.7 cm branch is fixed at 8.2 V (reference arm/arm 2) to get the minimum intensity at the OFF state.

Both the loss and phase components are taken into account to calculate the output transmission.

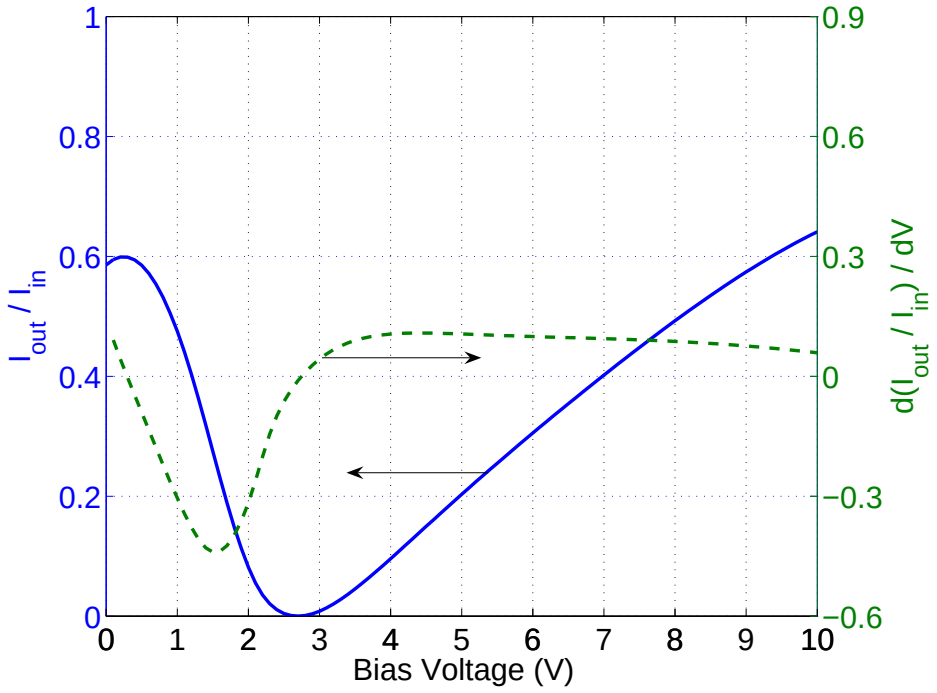

Figure 3.8: Ratio of output to input intensity in a MZI, dotted line shows the slope of this curve.

The ratio of output to input intensity as well as its slope as a function of the voltage on arm 1 are given in Fig. 3.8. At $V_{\text{arm1}} = 1.5V$ the slope of the I_{out}/I_{in} curve is very high (-0.43 V^{-1}). We can bias the modulating arm at this voltage and then apply a small-signal to this arm so that the output intensity will be varied in a small range. By doing this, the modulator will operate only in the quantum-well-modulation region rather than using the NID-layer-modulation.

3.4 Conclusion

In this chapter the performance of a single quantum-well modulator is discussed. During the DC analysis, from Fig. 3.3(a), we found that below 2 V the effective index variation in the single quantum-well structure is slightly higher than that in the 3 quantum-well structure. Fig. 3.3(b) shows that The highest slope of the effective index variation for the single quantum-well modulator occurs at about 1.6 V. We found that, if we desire a V_π below this voltage, it gives lower $V_\pi L_\pi$ as compared to the $V_\pi L_\pi$ of the 3 quantum-well modulator for both digital signal modulation and low voltage modulation.

Again, during the transient analysis, from Fig. 3.5, we found that most of the holes are removed from the quantum-well by $t = 36$ ps. We concluded from this figure that the hole depletion process is much faster in the case of the single quantum-well modulator than in the case of the 3 quantum-well modulator. The rise time and the fall time of the single quantum-well modulator, which we calculated from Fig. 3.7, were found to be around 3.02 ps and 2.25 ps, respectively, which are lower than that of the 3 quantum-well modulator. The performance of a Mach-Zehnder interferometer using single quantum-well phase modulators inserted into the two branches of the Mach-Zehnder interferometer were described next.

We can conclude with the idea that, if we want to operate in a lower bias region, we can remove the quantum-wells and only the highly doped P^+ layers and the NID layers may be sufficient to obtain an effective index variation close to that obtained with the 3 quantum-well or single quantum-well modulator in a lower bias region ($V < 2$ V). Removing the quantum-

wells from the modulator may also increase the intrinsic speed.

Chapter 4

Summary, Conclusion, and Suggestions for Future Work

4.1 Summary

In this thesis we described the electrical and optical analysis required for designing SiGe/Si quantum-well optical modulators. Then we studied the performance of a 3 quantum-well modulator based on this analysis. Then we designed a single quantum-well modulator which has lower $V_\pi L_\pi$ product, lower absorption losses, and higher intrinsic speed than the 3 quantum-well modulator.

In Chapter 2, **Material Choice, Device Structure, and Electrical and Optical Simulations**, we described the key components for designing SiGe/Si quantum-well modulators based on the free carrier depletion effect. The electrical and optical properties of Si and SiGe, which are important for designing these modulators were discussed at the beginning of Chapter 2. The software used for the electrical simulation of these modulators and the models used in this simulation was described next. Then, we discussed the mode solver program used for the optical simulation of SiGe/Si waveguide

modulators. The general structure of a $Si_{0.8}Ge_{0.2}$/Si quantum-well phase modulator followed by the coupled electrical-optical analysis used to design these modulators was presented next. Using this analysis, we simulated a 3 quantum-well $Si_{0.8}Ge_{0.2}$/Si modulator (designed by Marris *et al.*) providing the most important results of the simulations. The two most important performance parameters obtained for this modulator are the $V_\pi L_\pi$ product and the optical loss which are found to be around 2.039 V·cm for 0 to 6 V digital modulation and 5.75 dB/cm at $V = 0$ V for the wavelength of $\lambda_0 = 1.55$ μm. During the DC analysis, we found that below 1.5 V, the effective index variation Δn_{eff} is mainly caused by the refractive index change in the first quantum-well. The onset of the change in the refractive index in the second quantum-well occurs after the refractive index change in the first quantum-well approaches the saturation value. If we want to operate in a low bias region (below 1.5 V), only one quantum-well may be sufficient to have the same effective index variation as we obtained in the 3 quantum-well structure. Again, during the transient analysis, we found that by $t = 36$ ps and $t = 80$ ps the 1st and the 2nd quantum-wells are depleted, respectively. By $t = 100$ ps, only a few holes are left in the 3rd quantum-well. If we can get rid of the last 2 quantum-wells, the hole depletion process from the quantum-well could be done by $t = 36$ ps. From the results of the DC analysis and the transient analysis performed on this 3 quantum-well modulator, we came to the conclusion that, a single quantum-well modulator may have a lower drive voltage, lower optical loss, and be capable of higher intrinsic speed than the 3 quantum-well modulator. Hence we removed 2 quantum-wells from the 3 quantum-well modulator and designed a single

quantum-well modulator which was described in Chapter 3.

In Chapter 3, **Single Quantum-Well SiGe/Si Optical Modulator**, the results of the simulation on a single quantum-well $Si_{0.8}Ge_{0.2}$/Si modulator, which is derived from the 3 quantum-well modulator described in Chapter 2, was discussed. Then we compared its performance with that of the 3 quantum-well modulator and we found that, this single quantum-well modulator is better than the 3 quantum-well modulator in terms of the drive voltage, the optical loss, and the intrinsic speed. The $V_\pi L_\pi$ product of the single quantum-well modulator is estimated 1.09 V·cm for low voltage linear modulation and 1.208 V·cm for 0 to 1.6 V digital modulation, whereas the 3 quantum-well modulator gives a $V_\pi L_\pi$ of 2.039 V·cm for 0 to 6 V digital modulation for operation at $\lambda_0 = 1.55$ μm. Also, the optical loss in the single quantum-well (5.36 dB/cm at $V = 0$ V) is lower than that of the 3 quantum-well structure (5.75 dB/cm at $V = 0$ V). From the transient analysis of the electro-optic effect, we calculated the rise time and the fall time of both of the modulators. The rise time and the fall time of the single quantum-well modulator are found to be around 3.02 ps and 2.25 ps, respectively, whereas for the 3 quantum-well modulator these are found to be around 26.6 ps and 21 ps, respectively. The performance of a Mach-Zehnder interferometer using single quantum-well phase modulators inserted into the two branches of the Mach-Zehnder interferometer was described next. This chapter concluded with the idea that, if we want to operate in a lower bias region, we can remove the quantum-wells and only the highly doped P^+ layers and the NID layers are sufficient to obtain an effective index variation close to that obtained with the 3 quantum-well or single quantum-well

modulator in a lower bias region ($V < 2$ V). Removing the quantum-wells from the modulator may also increase the intrinsic speed.

4.2 Suggestions for Future Work

4.2.1 All-Silicon Optical Modulators

We want to simulate all-Si optical modulators and optimize those structures for getting lower $V_\pi L_\pi$, lower optical loss, and higher intrinsic speed. Currently we have two structures which we want to simulate in future.

The 1st device will consist of a P-I-N (P-Intrinsic-N) diode; the active region will consist of a 30 nm Si-NID layer surrounded by two 5 nm P^+ highly doped (2×10^{18} cm^{-3}) layers. The PIN diode will be placed on a 30 nm Si-NID layer at the bottom of the PIN diode. This structure will be simulated using a 2 μm SiO_2 layer.

The 2nd device will consist of a P-I-P-I-N diode laterally grown on a 2 μm SiO_2 layer. A 200 nm wide P layer, with a doping concentration of 10^{17} cm^{-3}, will be inserted into the intrinsic region of the P-I-N diode, giving the P-I-P-I-N structure. This P layer will be surrounded by two NID layers.

We expect that these devices can provide lower $V_\pi L_\pi$, lower optical loss, and higher intrinsic speed than those of the SiGe/Si quantum-well modulators.

4.2.2 Traveling-Wave Electrodes

In the case of the lumped electrodes, the speed of operation is limited by the RC time constants of the electrodes. Hence, we intend to investigate pos-

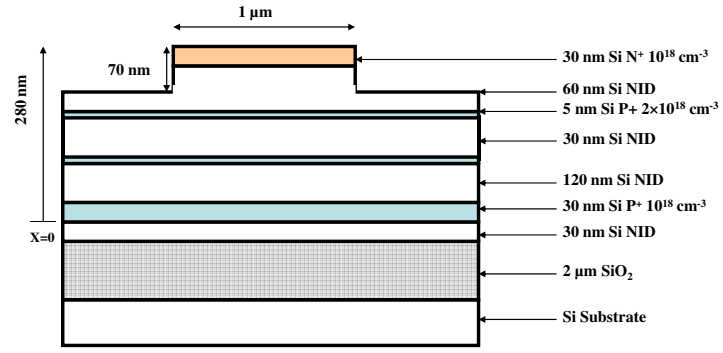

(a)

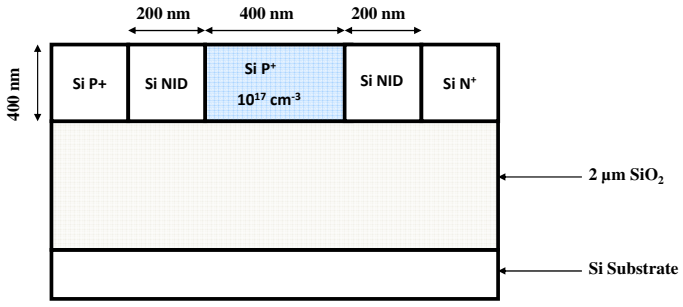

(b)

Figure 4.1: (a) All-Si optical modulator (vertical diode), (b) all-Si optical modulator (lateral diode).

sible improvement using slow-wave electrodes which remove this RC time constant dependency. The RF signal will be launched onto coplanar slow wave electrodes and co-propagate with the optical signal. The slow-wave electrodes will be designed using the EM simulation software SONNET with the goal of impedance matching, reducing the microwave-light velocity mismatch, and reducing the microwave loss.

Bibliography

[1] G. Chen, H. Chen, M. Haurylau, N. A. Nelson, D. H. Albonesi, P. M. Fauchet, and E. G. Friedman, "Predictions of CMOS compatible on-chip optical interconnect," *Integration, the VLSI Journal*, vol. 40, no. 4, pp. 434–446, Jul. 2007. [Online]. Available: http://www.sciencedirect.com/science/article/B6V1M-4MBTTVP-1/2/5701724f0d0cddc93f80bed02ecaa42e

[2] "Itrs2007." [Online]. Available: http://www.itrs.net/Links/2007ITRS/ExecSum2007.pdf

[3] L. Zheng and H. Tenhunen, "Wires as interconnects," in *Interconnect-Centric Design for Advanced SoC and NoC*, 2005, pp. 25–54. [Online]. Available: http://dx.doi.org/10.1007/1-4020-7836-6_2

[4] Y.-H. Kuo, "Germanium-silicon electroabsorption modulators," Ph.D. dissertation, Stanford University, 2006.

[5] B. Jalali, S. Yegnanarayanan, T. Yoon, T. Yoshimoto, I. Rendina, and F. Coppinger, "Advances in silicon-on-insulator optoelectronics," *Selected Topics in Quantum Electronics, IEEE Journal of*, vol. 4, no. 6, pp. 938–947, 1998.

[6] V. K. Yang, M. E. Groenert, G. Taraschi, C. W. Leitz, A. J. Pitera, M. T. Currie, Z. Cheng, and E. A. Fitzgerald, "Monolithic integration of III-V optical interconnects on si using SiGe virtual substrates," *Journal of Materials Science: Materials in Electronics*, vol. 13, no. 7, pp. 377–380, Jul. 2002. [Online]. Available: http://dx.doi.org/10.1023/A:1016006824115

[7] R. Soref and B. Bennett, "Electrooptical effects in silicon," *Quantum Electronics, IEEE Journal of*, vol. 23, no. 1, pp. 123–129, 1987.

[8] P. H. Wendland and M. Chester, "Electric field effects on indirect optical transitions in silicon," *Physical Review*, vol. 140, no. 4A, p. A1384, Nov. 1965, copyright (C) 2010 The American Physical Society; Please report any problems to prola@aps.org. [Online]. Available: http://link.aps.org/abstract/PR/v140/pA1384

[9] J. Roth, O. Fidaner, R. Schaevitz, Y. Kuo, T. Kamins, J. Harris, and D. Miller, "Optical modulator on silicon employing germanium quantum wells," *Opt. Express*, vol. 15, no. 9, pp. 5851–5859, 2007.

[10] V. I. Fistul', *Heavily doped semiconductors [by] Victor I. Fistul'.*, 418th ed., ser. English. (New York): Plenum Press, 1969. [Online]. Available: http://openlibrary.org/b/OL18665358M/Heavily_doped_semiconductors_by_Victor_I._Fistul%27.

[11] N. Dagli, *High-speed photonic devices.*, CRC Press, 2007.

[12] L. K. C. Lam, "A silicon guided-wave optical modulator using free- car-

rier dispersion effect and radiation loss mechanism," Ph.D. dissertation, University of Washington, 1997.

[13] E. Garmire and A. Kost, *Nonlinear Optics in Semiconductors II.*, Academic Press, Nov. 1998.

[14] W. Spitzer and H. Y. Fan, "Infrared absorption in n-Type silicon," *Physical Review*, vol. 108, no. 2, p. 268, Oct. 1957, copyright (C) 2010 The American Physical Society; Please report any problems to prola@aps.org. [Online]. Available: http://link.aps.org/abstract/PR/v108/p268

[15] W. C. Dash and R. Newman, "Intrinsic optical absorption in Single-Crystal germanium and silicon at 77K and 300K," *Physical Review*, vol. 99, no. 4, p. 1151, 1955, copyright (C) 2010 The American Physical Society; Please report any problems to prola@aps.org. [Online]. Available: http://link.aps.org/abstract/PR/v99/p1151

[16] P. E. Schmid, "Optical absorption in heavily doped silicon," *Phys. Rev. B*, vol. 23, no. 10, pp. 5531–5536, May 1981.

[17] J. Liu, M. Beals, A. Pomerene, S. Bernardis, R. Sun, J. Cheng, L. C. Kimerling, and J. Michel, "Waveguide-integrated, ultralow-energy GeSi electro-absorption modulators," *Nat Photon*, vol. 2, no. 7, pp. 433–437, Jul. 2008. [Online]. Available: http://dx.doi.org/10.1038/nphoton.2008.99

[18] L. Chao, "Silicon-based optical microresonator devices : polygonal mi-

crodisk channel filters and electro-optic modulators/switches," Ph.D. dissertation, Hong Kong University of Science and Technology, 2007.

[19] S. Bernardis, "Sige electro-absorption modulators for applications at 1550 nm," Master's thesis, Massachusetts Institute of Technology, 2008.

[20] S. Manipatruni, Q. Xu, B. Schmidt, J. Shakya, and M. Lipson, "High speed carrier injection 18 Gb/s silicon micro-ring electro-optic modulator," *Proc. of the IEEE Lasers and Electro-Optics Society*, pp. 537–538.

[21] L. Liao, D. Samara-Rubio, M. Morse, A. Liu, D. Hodge, D. Rubin, U. Keil, and T. Franck, "High speed silicon Mach-Zehnder modulator," *Optics Express*, vol. 13, no. 8, pp. 3129–3135, Apr. 2005. [Online]. Available: http://www.opticsexpress.org/abstract.cfm?URI=oe-13-8-3129

[22] A. Liu, L. Liao, D. Rubin, H. Nguyen, B. Ciftcioglu, Y. Chetrit, N. Izhaky, and M. Paniccia, "High-speed optical modulation based on carrier depletion in a silicon waveguide," *Optics Express*, vol. 15, no. 2, pp. 660–668, 2007. [Online]. Available: http://www.opticsexpress.org/abstract.cfm?URI=oe-15-2-660

[23] D. Marris-Morini, X. L. Roux, D. Pascal, L. Vivien, E. Cassan, J. M. Fdli, J. F. Damlencourt, D. Bouville, J. Palomo, and S. Laval, "High speed all-silicon optical modulator," *Journal of Luminescence*, vol. 121, no. 2, pp. 387–390, Dec. 2006. [Online]. Available: http://www.sciencedirect.com/science/article/B6TJH-4M1DB93-3/2/9ab0549731ed07f9913a750bc9a2d64f

[24] D. Marris-Morini, L. Vivien, J. M. Fdli, E. Cassan, P. Lyan, and S. Laval, "Low loss and high speed silicon optical modulator based on a lateral carrier depletion structure," *Optics Express*, vol. 16, no. 1, pp. 334–339, 2008. [Online]. Available: http://www.opticsexpress.org/abstract.cfm?URI=oe-16-1-334

[25] S. Maine, D. M. Morini, L. Vivien, E. Cassan, and S. Laval, "Design optimization of a SiGe/Si Quantum-Well optical modulator," *Journal of Lightwave Technology*, vol. 26, no. 6, pp. 678–684, Mar. 2008. [Online]. Available: http://jlt.osa.org/abstract.cfm?URI=JLT-26-6-678

[26] D. Marris, E. Cassan, L. Vivien, D. Pascal, A. Koster, and S. Laval, "Design of a modulation-doped SiGe/Si optical modulator integrated in a submicrometer silicon-on-insulator waveguide," *Optical Engineering*, vol. 44, no. 8, pp. 084 001–6, 2005. [Online]. Available: http://link.aip.org/link/?JOE/44/084001/1

[27] E. Cassan, S. Laval, D. Marris, M. Rouvire, L. Vivien, M. Halbwax, A. Lupu, and D. Pascal, "Active SiGe devices for optical interconnects," in *Optical Interconnects*, 2006, pp. 125–159. [Online]. Available: http://dx.doi.org/10.1007/978-3-540-28912-8_6

[28] S. Rihani, "SiGe strain tuning platforms: Material properties and advantages offered to the Si-based technology," *IBS Journal of Science*, vol. 2, no. 1, pp. 18–23, 2007.

[29] J. C. G. de Sande, A. Rodriguez, and T. Rodriguez, "Spectroscopic ellipsometry determination of the refractive index of strained si[sub

1 - x]Ge[sub x] layers in the near-infrared wavelength range (0.9–1.7 mu m)," *Applied Physics Letters*, vol. 67, no. 23, pp. 3402–3404, Dec. 1995. [Online]. Available: http://link.aip.org/link/?APL/67/3402/1

[30] *Properties of silicon germanium and SiGe:Carbon*, ser. English. (London): INSPEC, Institution of Electrical Engineers, 2000. [Online]. Available: http://openlibrary.org/b/OL22324731M/Properties_of_silicon_germanium_and_SiGe_Carbon

[31] "Silvaco Atlas software." [Online]. Available: http://www.silvaco.com/products/device_simulation/atlas.html

[32] P. Waldron, "Optimization of plasma dispersion modulators in silicon-on-insulator," Ph.D. dissertation, McMaster University, 2005.

[33] M. Grupen, K. Hess, and G. Song, "Simulation of transport over heterojunctions," in *Proc. 4th International Conf. Simul. Semicon. Dev. Process*, vol. 4, pp. 303–311.

[34] K. Horio and H. Yanai, "Numerical modeling of heterojunctions including the thermionicemission mechanism at the heterojunction interface," *IEEE Transactions on Electron Devices*, vol. 37, no. 4, pp. 1093–1098, 1990.

[35] A. Vonsovici and L. Vescan, "Modulation doped SiGe-Si MQW for low-voltage high-speed modulators at 1.3 m," *Selected Topics in Quantum Electronics, IEEE Journal of*, vol. 4, no. 6, pp. 1011–1019, 1998.

[36] S. Lardenois, D. Pascal, L. Vivien, E. Cassan, S. Laval, R. Orobtchouk,

M. Heitzmann, N. Bouzaida, and L. Mollard, "Low-loss submicrometer silicon-on-insulator rib waveguides and corner mirrors," *Optics Letters*, vol. 28, no. 13, pp. 1150–1152, Jul. 2003. [Online]. Available: http://ol.osa.org/abstract.cfm?URI=ol-28-13-1150

[37] A. Yariv and P. Yeh, *Photonics: Optical Electronics in Modern Communications*, 6th ed. Oxford University Press, USA, 2006.

[38] A. Fallahkhair, K. S. Li, and T. E. Murphy, "Vector finite difference modesolver for anisotropic dielectric waveguides," *Journal of Lightwave Technology*, vol. 26, no. 11, pp. 1423–1431, Jun. 2008. [Online]. Available: http://jlt.osa.org/abstract.cfm?URI=JLT-26-11-1423

[39] "Mode solver." [Online]. Available: http://www.photonics.umd.edu/software/wgmodes/

[40] D. Marris, E. Cassan, and L. Vivien, "Response time analysis of SiGe/Si modulation-doped multiple-quantum-well structures for optical modulation," *Journal of Applied Physics*, vol. 96, no. 11, pp. 6109–6112, Dec. 2004. [Online]. Available: http://link.aip.org/link/?JAP/96/6109/1

[41] I. Tan, G. L. Snider, L. D. Chang, and E. L. Hu, "A self-consistent solution of Schro?dingerCPoisson equations using a nonuniform mesh," *Journal of Applied Physics*, vol. 68, no. 8, p. 4071, 1990. [Online]. Available: http://link.aip.org/link/JAPIAU/v68/i8/p4071/s1&Agg=doi

[42] A. Lupu, D. Marris, D. Pascal, J. Cercus, A. Cordat, V. L. Thanh, and S. Laval, "Experimental evidence for index modulation by carrier depletion in SiGe/Si multiple quantum well structures," *Applied Physics Letters*, vol. 85, no. 6, pp. 887–889, 2004. [Online]. Available: http://link.aip.org/link/?APL/85/887/1

[43] "SiGe properties." [Online]. Available: http://www.virginiasemi.com/pdf/generalpropertiesSi62002.pdf

[44] A. Cordat, S. Lardenois, V. L. Thanh, and A. Koster, "SiGe/Si multiquantum well structure for light modulation," *Materials Science and Engineering B*, vol. 89, no. 1-3, pp. 66–69, Feb. 2002. [Online]. Available: http://www.sciencedirect.com/science/article/B6TXF-44YVPGS-G/2/267924d9f1f6ca50a49a33269efe277b

[45] T. E. Murphy, "Design, fabrication and measurement of integrated bragg grating optical filters," Ph.D. dissertation, Massachusetts Institute of Technology, 2001.

Appendix A

Mach-Zehnder Interferometer

An integrated Mach-Zehnder interferometer consists of an input waveguide, a splitter, two phase shifters, an output combiner, and an output waveguide, as illustrated in Fig. A.1. The optical beam coming through the input waveguide is split into two optical beams by the splitter. The two optical beams travel through the two phase shifters inserted into the arms of the Mach-Zehnder interferometer, and then recombine at the output combiner.

Assuming the waveguide Y-branch splitter at the input of the interferometer divides the wave evenly, the intensities in arm 1 and arm 2 of the interferometer will be the same. Suppose, the electric fields in arm 1 and arm 2 of the interferometer as E_1 and E_2 respectively.

$$E_{out} = \frac{E_1 + E_2}{\sqrt{2}} \tag{A.1}$$

Suppose k_1 and k_2, are the complex wavenumbers in arm 1 and arm 2, respectively, which can be expressed by

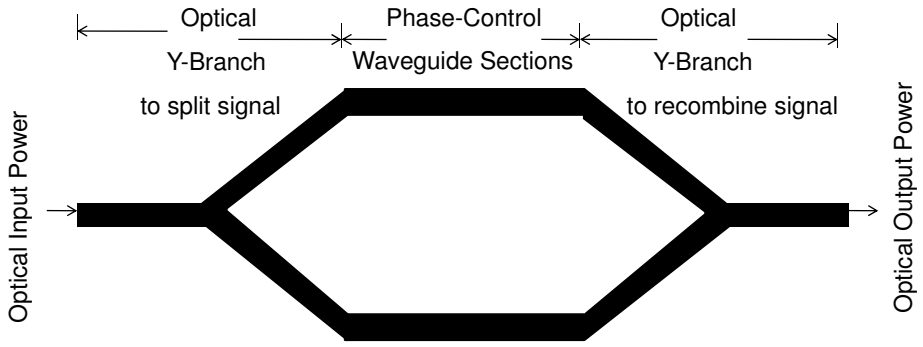

Figure A.1: Schematic view of the Mach-Zehnder interferometer. Two optical Y-branch couplers are used to split and recombine the incoming light.

$$k_1 = \beta_1 + i\alpha_1 = \beta_0 + \Delta\beta_1 + i\left(\frac{\alpha_0 - \Delta\alpha_1}{2}\right) \tag{A.2}$$

$$k_2 = \beta_2 + i\alpha_2 = \beta_0 + \Delta\beta_2 + i\left(\frac{\alpha_0 - \Delta\alpha_2}{2}\right) \tag{A.3}$$

where β_0 and α_0 is the propagation constant and the optical power absorption coefficient of light in both of the arms without the application of voltage. $\Delta\beta_1$ and $\Delta\alpha_1$ are the changes of propagation constant and absorption coefficient, respectively, in arm 1. $\Delta\beta_2$ and $\Delta\alpha_2$ are those changes in

arm 2.

$$E_{out} = \frac{E}{\sqrt{2}} \cdot e^{i(k_1 z_1 - \omega t)} + \frac{E}{\sqrt{2}} \cdot e^{i(k_2 z_2 - \omega t)} \tag{A.4}$$

$$E_{out} = \frac{E}{\sqrt{2}} \cdot e^{i(\beta_1 z_1 - \omega t)} \cdot e^{-\alpha_1 z_1/2} + \frac{E}{\sqrt{2}} \cdot e^{i(\beta_2 z_2 - \omega t)} \cdot e^{-\alpha_2 z_2/2} \tag{A.5}$$

$$P_{out} = E_{out} \cdot E^*_{out} \tag{A.6}$$

$$\begin{aligned} P_{out} =& \frac{E^2}{2} \cdot \left[e^{i(\beta_1 z_1 - \omega t)} \cdot e^{-\alpha_1 z_1/2} + e^{i(\beta_2 z_2 - \omega t)} \cdot e^{-\alpha_2 z_2/2} \right] \\ & \cdot \left[e^{-i(\beta_1 z_1 - \omega t)} \cdot e^{-\alpha_1 z_1/2} + e^{-i(\beta_2 z_2 - \omega t)} \cdot e^{-\alpha_2 z_2/2} \right] \end{aligned} \tag{A.7}$$

$$P_{in} = P_{in-1} + P_{in-2} = E^2 + E^2 = 2 \cdot E^2 \tag{A.8}$$

So,

$$\begin{aligned} P_{out} =& \frac{P_{in}}{4} \cdot \left[e^{i(\beta_1 z_1 - \omega t)} \cdot e^{-\alpha_1 z_1/2} + e^{i(\beta_2 z_2 - \omega t)} \cdot e^{-\alpha_2 z_2/2} \right] \\ & \cdot \left[e^{-i(\beta_1 z_1 - \omega t)} \cdot e^{-\alpha_1 z_1/2} + e^{-i(\beta_2 z_2 - \omega t)} \cdot e^{-\alpha_2 z_2/2} \right] \end{aligned} \tag{A.9}$$

$$\begin{aligned} P_{out} =& \frac{P_{in}}{4} \cdot \left[e^{i(\beta_1 z_1 - \omega t)} \cdot e^{-\alpha_1 z_1/2} + e^{i(\beta_2 z_2 - \omega t)} \cdot e^{-\alpha_2 z_2/2} \right] \\ & \cdot \left[e^{-i(\beta_1 z_1 - \omega t)} \cdot e^{-\alpha_1 z_1/2} + e^{-i(\beta_2 z_2 - \omega t)} \cdot e^{-\alpha_2 z_2/2} \right] \end{aligned} \tag{A.10}$$

$$P_{out} = \frac{P_{in}}{4} \cdot \left[e^{-\alpha_1 z_1} + e^{-\alpha_2 z_2} + e^{i(\beta_2 z_2 - \beta_1 z_1)} \cdot e^{-\alpha_1 z_1/2 + \alpha_2 z_2/2} + e^{i(\beta_1 z_1 - \beta_2 z_2)} \cdot e^{-\alpha_1 z_1/2 + \alpha_2 z_2/2} \right] \tag{A.11}$$

$$\frac{P_{out}}{P_{in}} = \frac{1}{4} \left[e^{-\alpha_1 z_1} + e^{-\alpha_2 z_2} + 2 \cdot e^{-\alpha_1 z_1/2 + \alpha_2 z_2/2} \cdot cos\left(\beta_2 z_2 - \beta_1 z_1\right) \right] \tag{A.12}$$

$$\frac{I_{out}}{I_{in}}(V) = \frac{1}{4} \left[e^{-\alpha_1(V) z_1} + e^{-\alpha_2(V) z_2} + 2 \cdot e^{-\alpha_1 z_1/2 + \alpha_2 z_2/2} \cdot cos\left(\beta_2(V) z_2 - \beta_1(V) z_1\right) \right] \tag{A.13}$$

Appendix B

Mode Solver Program

The description of the mode solver used to solve for the eigen modes in the SOI waveguides is described in detail in [38, 45]. In this appendix, we will describe the mode solver very briefly.

The full-vector eigen value equation which describes the modes of propagation for an integrated waveguide is given by-

$$\begin{Vmatrix} P_{xx} & P_{xy} \\ P_{yx} & P_{yy} \end{Vmatrix} \begin{Vmatrix} e_x \\ e_y \end{Vmatrix} = \beta^2 \begin{Vmatrix} e_x \\ e_y \end{Vmatrix} \tag{B.1}$$

where $P_{xx}...P_{yy}$ are differential operators defined as-

$$P_{xx}e_x = \frac{\delta}{\delta x}\left[\frac{1}{n^2}\frac{\delta(n^2 e_x)}{\delta x}\right] + \frac{\delta^2 e_x}{\delta y^2} + n^2k^2e_x \tag{B.2}$$

$$P_{yy}e_y = \frac{\delta}{\delta y}\left[\frac{1}{n^2}\frac{\delta(n^2 e_y)}{\delta y}\right] + \frac{\delta^2 e_y}{\delta x^2} + n^2k^2e_y \tag{B.3}$$

$$P_{xy}e_y = \frac{\delta}{\delta x}\left[\frac{1}{n^2}\frac{\delta n^2 e_y}{\delta y}\right] - \frac{\delta^2 e_y}{\delta x \delta y} \tag{B.4}$$

$$P_{yx}e_x = \frac{\delta}{\delta y}\left[\frac{1}{n^2}\frac{\delta n^2 e_x}{\delta x}\right] - \frac{\delta^2 e_x}{\delta y \delta x} \tag{B.5}$$

where n and β, respectively, denote the refractive index of the layers in

the waveguide and the propagation constant of the eigen mode. The two transverse electric field components, e_x and e_y, are the eigenfunctions, and the corresponding eigenvalue is β^2. The four remaining field components e_z, h_x, h_y, and h_z are derived from these two transverse components by applying Maxwell's equations. The two transverse field components e_x and e_y are coupled, i.e. these cannot be solved separately by two separate eigen value equations. Because of this coupling, the eigenmodes of an optical waveguide are usually not purely TE or TM modes, and they are often referred to as hybrid modes [45]. However, in our simulations, we assumed that one of the two transverse field components is larger than the other, and we used the semivectorial finite difference method which neglects the smaller field component and solves the eigenvalue equations for the remaining field component by neglecting P_{xy}, P_{yx} and either P_{xx} or P_{yy} in the full vector finite difference method which is described in [45]. For example, if we want to solve for e_x, The eigen value equation is reduced to the semivectorial eigen value equation which is

$$P_{xx}e_x = \beta^2 e_x \tag{B.6}$$

$$\left(\frac{\delta^2}{\delta x^2} + \frac{\delta^2}{\delta y^2} + n^2(x,y)k^2\right) e_x = \beta^2 e_x \tag{B.7}$$

The ridge waveguide is broken up into small rectangular cells or pixels of size $\Delta x \times \Delta y$. In each cell, refractive index is constant and the discontinuities in the refractive index may occur at the boundaries of the pixel. This is illustrated in Fig. B.1. For every grid point located at the center of each

cell, the partial differential equation is translated into a finite difference equation. Suppose for the point P, Equation B.7 will be turned into the difference equation [45]:

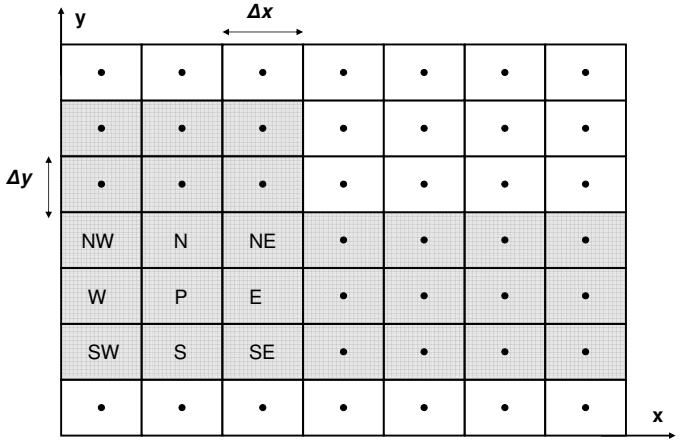

Figure B.1: A typical finite difference mesh for an integrated waveguide. The rib waveguide is shown by the shaded region. P, N, S, E, W, NE, NW, SE and SW are used to label, respectively, the grid point under consideration, and its nearest neighbours to the north, south, east, west, north-east, north-west, south-east, and south-west.

$$\frac{\phi_W}{(\Delta x)^2} + \frac{\phi_E}{(\Delta x)^2} + \frac{\phi_N}{(\Delta y)^2} + \frac{\phi_S}{(\Delta y)^2} + \left(n_P^2 k^2 - \frac{2}{(\Delta x)^2} - \frac{2}{(\Delta y)^2} \right) \phi_P = \beta^2 \phi_P \tag{B.8}$$

where ϕ_P is the field sample at the grid point P and ϕ_N, ϕ_S, ϕ_E, ϕ_W are the field samples at the grid points immediately north, south, east, and west of the point under consideration, P. Thus the eigen function e_x in equation B.7 is replaced by samples of field located at discrete grid points and the

operator P_{xx} can be represented by the following diagram which illustrates the coefficients we have to multiply with each of the sample points adjacent to a particular grid point.

0	$\frac{1}{(\Delta y)^2}$	0
$\frac{1}{(\Delta x)^2}$	$n_P^2 k^2 - \frac{2}{(\Delta x)^2} - \frac{2}{(\Delta y)^2}$	$\frac{1}{(\Delta x)^2}$
0	$\frac{1}{(\Delta y)^2}$	0

If we apply equation B.8 for each grid point in the computational window, we obtain an M number of eigenvalue equations, where M is the total number of the grid points. After constructing the sets of eigen value equations, boundary conditions will be considered for points which lie on the edge of the computation window. There can be three boundary conditions: absorbing, symmetric, and antisymmetric. By "absorbing", we mean that the field is assumed to be zero at grid points immediately outside a certain boundary of the computation window. By "symmetric" (or "antisymmetric"), we mean that the field is assumed to be symmetric (or "antisymmetric") at grid points immediately outside a certain boundary of the computation window. The modifications of the P_{xx} operator at the boundaries according to different boundary conditions are discussed in detail in [45].